

1 **In-situ estimation of soil hydraulic and hydrodispersive properties by**  
2 **inversion of Electromagnetic Induction measurements and soil**  
3 **hydrological modelling**

4 Giovanna Dragonetti<sup>1,Ψ</sup>, Mohammad Farzamian<sup>2,3,Ψ</sup>, Angelo Basile<sup>4</sup>, Fernando  
5 Monteiro Santos<sup>3</sup>, Antonio Coppola<sup>5,6</sup>

6 <sup>1</sup>Mediterranean Agronomic Institute of Bari, Valenzano (BA), 70010, Italy

7 <sup>2</sup>Instituto Nacional de Investigação Agrária e Veterinária, Oeiras, 2780-157, Portugal

8 <sup>3</sup>Instituto Dom Luiz, Faculdade de Ciências da Universidade de Lisboa, Lisboa, 1749-016, Portugal

9 <sup>4</sup>Institute for Mediterranean Agricultural and Forestry Systems, National Research Council, Portici (NA),  
10 80055, Italy

11 <sup>5</sup>School of Agricultural, Forestry, Food and Environmental Sciences, University of Basilicata, Potenza,  
12 85100, Italy

13 <sup>6</sup>[Department of Chemical and Geological Sciences, University of Cagliari, Cagliari, 09124, Italy](#)

14 **Ψ** These authors contributed equally to this work.

15 **Correspondence:** Mohammad Farzamian ([mohammad.farzamian@iniav.pt](mailto:mohammad.farzamian@iniav.pt)) and Giovanna Dragonetti  
16 ([dragonetti@iamb.it](mailto:dragonetti@iamb.it))

17

18 **ABSTRACT**

19 Soil hydraulic and hydrodispersive properties are necessary for modelling water and solute  
20 fluxes in agricultural and environmental systems. Despite the large efforts in developing methods  
21 (e.g. lab-based, [PpedotTransfer functionsF](#)), their characterization at applicative scales is still an  
22 imperative requirement. Accordingly, this paper proposes a non-invasive in situ method  
23 integrating Electromagnetic Induction (EMI) and hydrological modelling to estimate soil hydraulic  
24 and transport properties at the plot scale. To this aim, we carried out two sequential water  
25 infiltration and solute transport experiments and conducted time-lapse EMI surveys using a CMD

26 mini-Explorer to examine how well this methodology can be used to i) monitor water content  
27 dynamic after irrigation and to estimate the soil hydraulic van Genuchten–Mualem parameters  
28 from the water infiltration experiment and ii) to monitor solute concentration, and to estimate  
29 solute dispersivity from the solute transport experiment. We then compared the obtained results to  
30 those estimated by direct Time Domain reflectometry (TDR) and tensiometer probes  
31 measurements. The EMI significantly underestimated the water content distribution observed by  
32 TDR, but the water content evolved similarly over time. This introduced two main effects on soil  
33 hydraulic properties obtained by the two methods: i) Similar water retention curve shapes, but  
34 underestimated saturated water content from the EMI method, resulting in a scaled water retention  
35 curve when compared with the TDR method; the EMI-based water retention curve can be scaled  
36 by measuring the actual saturated water content at the end of the experiment with TDR probes or  
37 by weighing soil samples; ii) almost overlapping hydraulic conductivity curves, as expected when  
38 considering that the shape of the hydraulic conductivity curve primarily reflects changes in water  
39 content over time. Nevertheless EMI-based estimations of soil hydraulic properties and transport  
40 properties were found to be fairly accurate in comparison to those obtained from direct TDR  
41 measurements and tensiometer probes measurements.

42 ~~We then compared the obtained results to those estimated by direct TDR and tensiometer~~  
43 ~~probes measurements. Our results show a good agreement between EMI based estimation of soil~~  
44 ~~hydraulic and transport properties with those obtained from the direct TDR and tensiometer probes~~  
45 ~~measurements. When compared with direct TDR measurements, the EMI significantly~~  
46 ~~underestimated the water content distribution, but the water content evolved similarly over time.~~  
47 ~~This did not have a significant impact on the hydraulic conductivity curves since the hydraulic~~  
48 ~~conductivity is mainly a function of water content variation, not its absolute value. On the other~~

49 ~~hand, this underestimation led to lower saturated water content, reflected in the water retention~~  
50 ~~curve. The latter can be scaled by measuring the actual saturated water content at the end of the~~  
51 ~~experiment with TDR probes or even by weighing soil samples.~~

52

## 53 **1. INTRODUCTION**

54 Dynamics agro-hydrological models are more and more used for interpreting and solving agro-  
55 environmental problems (Hansen et al., 2012; Coppola et al., 2015; Kroes et al., 2017; Coppola et  
56 al., 2019). The soil hydrological component of these models is frequently based on mechanistic  
57 descriptions of water and solute fluxes in soils. Richards equation (RE) for water flow and  
58 Advection-Dispersion equation (ADE) for solute transport is generally accepted to apply at a local  
59 scale (plot scale, for example). Solving RE requires the determination of the hydraulic properties,  
60 namely the water retention curve relating the soil water content,  $\theta$ , to the soil water pressure head,  
61  $h$ , and the hydraulic conductivity curve, relating the hydraulic conductivity,  $K$  to either the water  
62 content,  $\theta$  or the pressure head,  $h$ . Similarly, ADE requires the dispersivity,  $\lambda$ , to be also known.  
63 In the last decades several laboratory and in-situ methods have been developed for characterizing  
64 soil hydraulic properties (e.g. Dane and Topp, 2020) and dispersive properties (e.g. Vanderborght  
65 and Vereecken, 2007). Lab-based characterizations may be carried out under more controlled  
66 conditions. Nevertheless, for simulating water and solute dynamics in the real field context, the in-  
67 situ methods are obviously more representative than the lab ones. This is firstly related to the size  
68 of the volume investigated, which has to appropriately represent the heterogeneity of the medium  
69 being studied (Wessolek et al., 1994; Ellsworth et al., 1996; van Genuchten et al., 1999; Inoue et  
70 al., 2000). Actually, a water flow process observed in situ will be influenced by the heterogeneities  
71 (stones, macropores, etc.) found in the field. This is the main limitation of the relatively small soil

72 columns generally analysed in the laboratory. By contrast, an in-situ characterization method, for  
73 example the well-known instantaneous profile method (Watson et al., 1966), can catch the  
74 hydraulic properties which are effective in describing the flow process observed in-situ. This will  
75 also depend on the measurement scale (the size of the plot) and on the observation scale of the  
76 sensors used. These issues have been dealt with in detail for example in Coppola et al. (2012;  
77 2016) and in Dragonetti et al., (2018). Besides, the experimental boundary conditions used to carry  
78 out the hydraulic characterization in lab and in-situ may also induce a different shape of the  
79 hydraulic properties as determined in the lab and in-situ (Basile et al., 2006).

80 In-situ methods typically evaluate soil hydraulic properties by monitoring an infiltration and/or  
81 a redistribution water flow process (Watson et al., 1966). Similarly, in situ methods for  
82 determining hydro-dispersive parameters are generally based on monitoring of mixing processes  
83 following pulse or step inputs of a tracer on either large plots or along field transect (Severino et  
84 al., 2010; Coppola et al., 2011; Vanderborght and Vereecken, 2007). Inverse modelling is  
85 frequently used to estimate the hydraulic and transport parameters simultaneously (Šimůnek et al.,  
86 1998a; Abbasi et al., 2003; Groh et al., 2018). Yet, even by shortening the measurement procedure  
87 by simplified assumptions (e.g. Sisson and van Genuchten 1991; Basile 2006) all in-situ methods  
88 for the characterization of the whole soil profile remain extremely difficult to implement also  
89 because they generally require installing sensors at different depths (e.g. TDR probes,  
90 tensiometers, access tubes for neutron probe) which are cumbersome and may induce soil  
91 disturbance, unless the installation is made much earlier than the experiment, to at least partly  
92 allowing the soil to recover through several wetting-drying cycles its natural structure.

93 In this direction, geophysical non-invasive methods based on the electrical resistivity  
94 tomography (ERT) and Electromagnetic Induction (EMI) techniques represent a promising

95 alternative to traditional sensors for soil hydraulic and transport parameters assessment. Many  
96 researchers have used the time-lapse ERT data (e.g. Binley et al., 2002; Kemna et al., 2002; Singha  
97 and Gorelick, 2005) to monitor ~~temporal~~ water content and saline tracer in the field~~solute~~  
98 ~~concentration changes in flow and transport models~~. The dependence of soil electrical conductivity  
99 on soil water content and concentration is the key mechanism that permits the use of time-lapse  
100 ERT to monitor water and solute dynamics in time-lapse mode along a soil profile, by relating  
101 resistivities to water contents and solute concentration distributions through empirical or semi-  
102 empirical relationships (e.g. Archie, 1942) or established in-situ relationships (e.g. Binley et al.,  
103 2002).

104 Electromagnetic induction (EMI) sensors may be also used ~~as an alternative to the ERT~~  
105 ~~technique~~ as they allow for monitoring water and solute propagation through a soil profile by  
106 simply moving the sensor above the soil surface without the need to install electrodes, as required  
107 by ERT technique. An EMI sensor provides measurements of the depth-weighted apparent  
108 electrical conductivity ( $\sigma_a$ ) according to the specific distribution of the bulk electrical conductivity  
109 ( $\sigma_b$ ), as well as the depth response function of the sensor used (McNeill, 1980).  $\sigma_a$  obtained from  
110 EMI sensors have been used to map the geospatial and temporal variability of the soil water content  
111 and salinity (Corwin and Lesch, 2005; Bouksila et al. 2012; Saeed et al., 2017). However,  
112 monitoring the propagation of the water and solutes with depth along a soil profile (as during a  
113 water infiltration or a solute transport experiment) requires the distribution of the  $\sigma_b$  distribution  
114 with depth to be known over time, which can be obtained by inversion of the  $\sigma_a$  observations from  
115 the EMI sensor (see for example, ~~Borchers et al., 1997~~; Hendrickx et al., 2002; Lavoué et al., 2010;  
116 ~~Mester et al., 2011~~; Deidda et al., 2014; Von Hebel et al., 2014; Dragonetti et al., 2018; Moghadas  
117 et al., 2019; Farzamian et al., 2019a; Zare et al. 2020; Mclachlan et al. 2020). More recently, this

118 inversion has been facilitated by the development of multi-coil EM sensors which are designed to  
119 collect  $\sigma_a$  at multiple coil spacing and orientations simultaneously in one sensor reading. This  
120 allows a rapid investigation of the soil's electrical conductivity at several depth ranges to obtain  
121 soil water content (Huang et al., 2016; Whalley et al., 2017) and solute concentrations (Paz et al.,  
122 2020; Gomez Flores et al., 2022) quickly and cheaply. However, the potential of EMI sensors to  
123 assess soil hydraulic and hydro-dispersive parameters has not been yet studied due to the lack of  
124 high-resolution and well-controlled experiments, required to catch the complexity of water flow  
125 and transport process during infiltration experiments.

126 With these premises, in this paper we propose a procedure based on a sequence of water  
127 infiltration and solute transport experiments, both monitored by an EMI sensor, with the objective  
128 of estimating in-situ the parameters of soil hydraulic properties and the dispersivity of a soil profile  
129 with a non-invasive EMI sensor and relatively short experiments at the plot scale. The sequence  
130 of water and solute infiltration has the main aim to discriminate the contribution of the water  
131 content and the soil solution electrical conductivity to the EMI-based  $\sigma_b$ . All the EMI data will be  
132 analysed by a hydrological model within a so-called uncoupled framework, ~~which will be~~  
133 ~~discussed in detail in the Hydro-Geophysical uncoupled approach section~~. The goodness of the  
134 adopted approach will be evaluated by comparing the EMI-based hydraulic and hydrodispersive  
135 properties to those obtained from in-situ TDR and tensiometer measurements. ~~The Our~~ aim is to  
136 explore an approach that does ~~not~~ need sensors installation and minimise data necessary for the  
137 in-situ assessment of soil hydraulic and hydrodispersive properties.

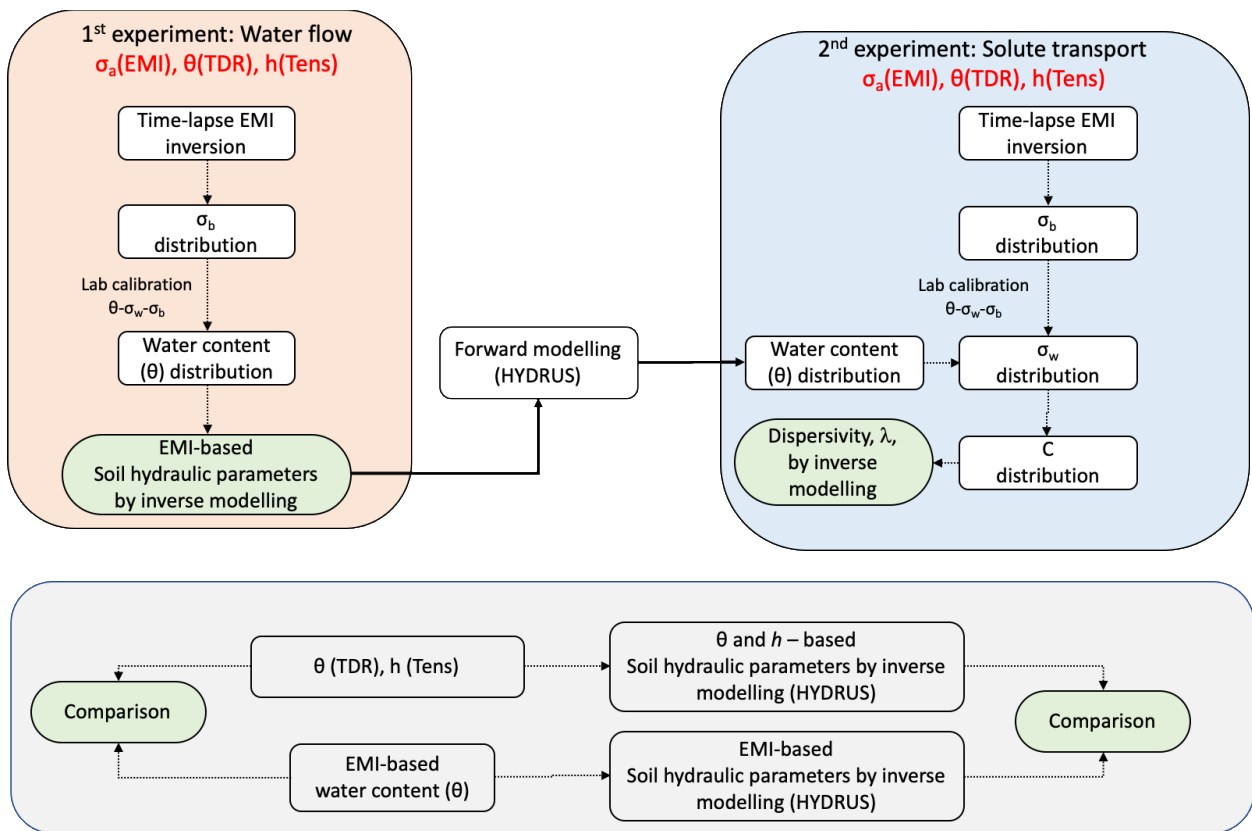
138

## 139 2. HYDRO-GEOPHYSICAL UNCOUPLED APPROACH

140 Figure 1 provides a schematic view of a six-step (+ one step for comparison) procedure, based  
141 on an uncoupled approach (Camporese et al., 2015) which will be adopted in this work to estimate  
142 the soil hydraulic and hydrodispersive properties using the data obtained from the EMI sensor. All  
143 the steps summarised below will be described in detail in the Materials and Methods section.

- 144 (i) Inversion of time-lapse  $\sigma_a$  EMI data obtained during (i) a water infiltration experiment,  
145 hereafter 1<sup>st</sup> experiment, and (ii) a subsequent solute transport experiment, hereafter 2<sup>nd</sup>  
146 experiment, to generate EMI-based  $\sigma_b$  distributions for each experiment;
- 147 (ii) Laboratory calibration of the relationship  $\theta$ - $\sigma_b$ - $\sigma_w$  in order to convert  $\sigma_b$  distributions to water  
148 content,  $\theta$ , (1<sup>st</sup> experiment) and to soil solution electrical conductivity,  $\sigma_w$ , and therefore  
149 solute concentrations,  $C$ , (2<sup>nd</sup> experiment);
- 150 (iii) Converting the  $\sigma_b$  distributions obtained from the 1<sup>st</sup> experiment to water content  
151 distributions, using the  $\theta$ - $\sigma_b$ - $\sigma_w$  relationship, to be used in the next numerical simulation step;
- 152 (iv) Numerical simulation, by using the HYDRUS-1D model (Šimůnek et al., 1998b), of the 1<sup>st</sup>  
153 experiment in order to estimate the van Genuchten-Mualem (vG-M) parameters through an  
154 inversion procedure based on the water contents inferred from step (iii);
- 155 (v) Conversion of the  $\sigma_b$  distributions obtained from the 2<sup>nd</sup> experiment to solute concentration  
156 distribution in order to estimate longitudinal dispersivity,  $\lambda$ . In this step,  $\sigma_w$  distribution was  
157 estimated by using the laboratory  $\theta$ - $\sigma_b$ - $\sigma_w$  calibration. The  $\theta$  distribution in the 2<sup>nd</sup>  
158 experiment was simulated based on the vG-M parameters obtained in step (iv). This is a  
159 crucial step in the proposed procedure, as it allows to discriminate the contribution of the  
160 soil water electrical conductivity, and thus of the solute concentration, to the  $\sigma_b$  EMI readings  
161 during the 2<sup>nd</sup> experiment. The  $\sigma_w$  distributions were thus converted to solute concentration  
162 by a simple standard lab-based solute specific  $\sigma_w$ - $C$  relationship;

- 163 (vi) Numerical simulation of the second solute infiltration process in order to estimate  $\lambda$  through  
 164 an inversion procedure based on the concentrations obtained from step (v).  
 165 (vii) An alternative dataset of  $\theta$  and  $\sigma_b$  obtained from direct TDR measurements, as well as  
 166 tensiometer pressure head ( $h$ ) readings, collected during the two experiments, allowed us to  
 167 obtain independent hydraulic and hydrodispersive properties (hereafter TDR-based for sake  
 168 of simplicity) to be used as a reference to evaluate the EMI-based parameter estimation (see  
 169 the horizontal grey box in Fig. 1).



170  
 171 Figure 1: Schematic diagram of the proposed Hydro-Geophysical uncoupled approach

172  
 173 **3. MATERIAL AND METHODS**  
 174 **3.1. Study area**



175 The experiment was performed at the Mediterranean Agronomic Institute of Bari (CIHEAM-  
176 IAM), south-eastern coast of Italy. The study area is located at an altitude of 72 m with 41° 3'  
177 13.251" N, a longitude of 16° 52' 36.274" E, ~~and an elevation of about 68 m a.s.l.~~ with a typical  
178 Mediterranean climate with rainy winters and very hot dry summers. The soil is a Colluvic Regosol  
179 consisting of silty loam layers of an average depth of 70 cm on a shallow fractured calcareous  
180 rock. Two main horizons on the calcareous rock may be identified: an Ap horizon (depth 0-30 cm)  
181 and a Bw horizon (depth 30-70 cm). Scattered calcareous fragments are present due to the breaking  
182 and grinding of the bedrock operated in the past by using heavy machinery in order to improve the  
183 soil structure and increase the soil depth for plantation

184

### 185 **3.2. Experimental set-up**

186 A layout of the experimental setup is shown in Fig. 2. The plot size is 4 × 4 m. Water was  
187 applied by using a drip irrigation system consisting of 20 lines, with drippers spaced 0.20 m and  
188 delivering a nominal flow rate of 10 l h<sup>-1</sup>. Thus 400 drippers were installed, capable of delivering  
189 4000 l h<sup>-1</sup> on the whole plot. The dripper's grid spacing and the flow rate were selected to ensure  
190 that a 1D flow field rapidly developed after starting irrigation. The drip irrigation system was  
191 placed on a metallic grid to be easily moved away from the plot and whenever EMI measurements  
192 were taken on the ground soil.

193 Several months before starting the 1<sup>st</sup> experiment, after digging a small pit, eight three-wire  
194 TDR probes, 7 cm long, 2.5 cm internal distance, and 0.3 cm in diameter, were inserted  
195 horizontally at 2 depths – 20 and 40 cm, corresponding to the Ap and the Bw horizon – in the 4  
196 corners of the experimental plot (at 1 m distance from the plot edge), as shown in Fig. 2. The pits  
197 for installing the sensors were refilled immediately, to leave some natural wetting and drying

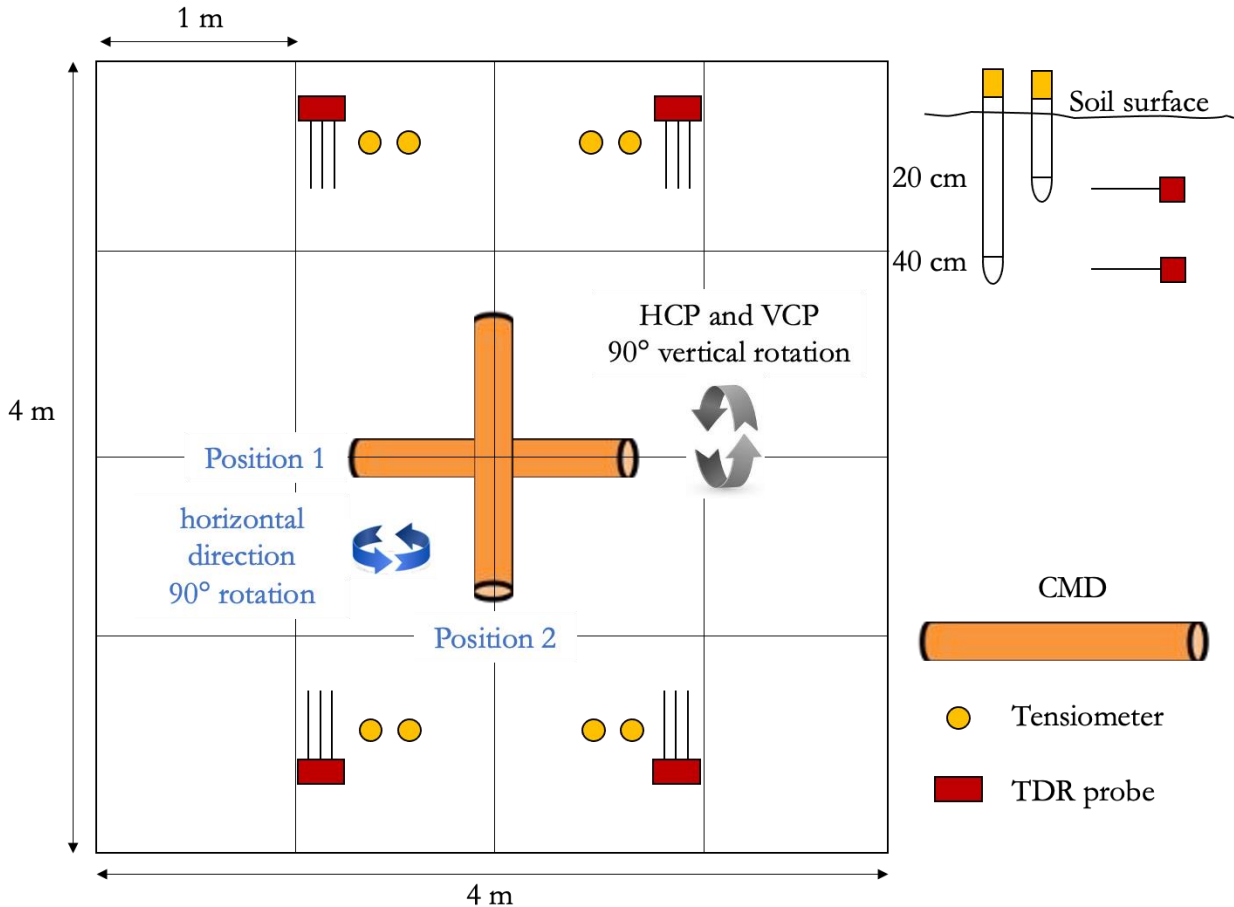
198 cycles to reproduce the original soil aggregation. Then, the plot was covered with a plastic sheet  
199 about four days prior to the start of the experiment to keep the plot under quasi-equilibrium  
200 conditions at the beginning of the experiment.

201 A Tektronix 1502C cable tester (Tektronix Inc., Baveron, OR) was used in this study, enabling  
202 simultaneous measurement of water content,  $\theta$ , and bulk electrical conductivity,  $\sigma_b$ , of the soil  
203 volume explored by the probe (Robinson et al., 2003; Coppola et al., 2011; 2013). Furthermore,  
204 eight tensiometers were vertically inserted near each TDR probe to acquire water potentials by a  
205 Tensicorder sensor (Hydrosense3 SK800). Both TDR probes and tensiometers were installed for  
206 the evaluation of the EMI-based parameter estimation (step (vii)).

207 The experimental plot was firstly irrigated by using tap water with an electrical conductivity  
208 of about  $1 \text{ dS m}^{-1}$  (1<sup>st</sup> experiment). We applied eleven irrigations, each lasting about 3 minutes to  
209 deliver about 180 l on the whole  $16 \text{ m}^2$  plot for each irrigation (the volume was measured by a  
210 flowmeter). Irrigations were separated by about a 1-hour shutoff. At each irrigation starting, due  
211 to the short inertia of the irrigation system just after its switching on, for some seconds drippers  
212 delivered less than  $10 \text{ l h}^{-1}$ . For each irrigation an average flow rate of about  $0.375 \text{ cm min}^{-1}$  was  
213 applied, which generated a small ponding at the soil surface for a short time. Overall, an average  
214 water volume of 2000 l was supplied.

215 The propagation of the wetting front along the soil profile was monitored by using an EMI  
216 sensor (i.e. CMD mini-Explorer, GF Instruments, Czech Republic), positioned horizontally in the  
217 middle of the plot (Fig. 2) in order to measure the apparent electrical conductivity,  $\sigma_a$ , in the soil  
218 profile in VCP (vertical coplanar, i.e., horizontal magnetic dipole configuration) mode and then  
219 HCP (horizontal coplanar, i.e., vertical magnetic dipole configurations) mode by rotating the probe  
220  $90^\circ$  axially to change the orientation from VCP to HCP mode. The CMD Mini-Explorer operates

221 at 30 kHz frequency and has three receiver coils with 0.32, 0.71 and 1.18 m distances from the  
222 transmitter coil, referred to hereafter as  $\rho_{32}$ ,  $\rho_{71}$ , and  $\rho_{118}$ . The manufacturer indicates that the  
223 instrument has an effective depth range of 0.5, 1.0 and 1.8 m in the HCP mode, which is reduced  
224 to half (0.25, 0.5, and 0.9 m) by using the VCP orientation. As a consequence, this EMI sensor  
225 returns six different  $\sigma_a$  values (utilizing three offsets with two coil orientations) with each  
226 corresponding to different depth sensitivity ranges. All measurements were performed five  
227 minutes after each water pulse application by temporarily removing the irrigation grid and placing  
228 the EMI sensor in the middle of the plot. The infiltration was also monitored by TDR probes and  
229 tensiometers in order to monitor the space-time evolution of water content,  $\theta$ , pressure head,  $h$ , as  
230 well as bulk electrical conductivity,  $\sigma_b$ . The distance of the TDR probes and tensiometers to the  
231 middle of the plot was specifically designed to avoid any interference with the EMI measurements.



232

233 Figure 2. Layout of the experimental and monitoring set-up. HCP (horizontal coplanar) and VCP  
 234 (vertical coplanar) are the vertical and horizontal dipolar orientations of the CMD probes,  
 235 respectively.

236

237 At the end of the 1<sup>st</sup> experiment, the soil was allowed to dry and then covered with a plastic  
 238 sheet to bring the distribution of water content along the profile similar to the initial one (observed  
 239 before the water infiltration test). Afterward, a similar infiltration experiment (2<sup>nd</sup>) was carried out  
 240 but using saline water at an electrical conductivity of 15 dS m<sup>-1</sup>, and obtained by mixing CaCl<sub>2</sub>  
 241 into the tap water. Again, eleven saline water supplies were provided at intervals of about 1 h apart  
 242 and a total volume of 2000 l saline water was supplied during the experiment. The propagation of

243 the water and chloride during the 2<sup>nd</sup> infiltration experiment was monitored similarly to the 1<sup>st</sup>  
244 experiment using TDR probes, tensiometers, and the CMD Mini-Explorer sensor.

### 245 **3.3. Site-specific calibration $\theta$ - $\sigma_b$ - $\sigma_w$**

246 The relationship between the bulk electrical conductivity ( $\sigma_b$ ), the electrical conductivity of the  
247 soil solution soil water ( $\sigma_w$ ), and the water content, were obtained by using the model proposed by  
248 Malicki and Walczak, (1999):

$$249 \sigma_w = \frac{\sigma_b - a}{(\epsilon_b - b)(0.0057 + 0.000071 S)} \quad (1)$$

250 where  $\epsilon_b$  (-) is the dielectric constant, which is related to the water content and  $S$  is the sand content  
251 in percent. The parameters  $a = 3.6 \text{ dS m}^{-1}$  and  $b = 0.11$  were obtained in a laboratory experiment  
252 reported in Farzamian et al. (2021). [Topp's equation was used to relate dielectric constant to the](#)  
253 [volumetric water content \(Topp et al., 1980\).](#) The lab experiment for such a calibration is quite  
254 simple, fast, and standard procedure on reconstructed soil samples. An additional linear  
255 calibration, obtained by using solutions at different concentrations of calcium chloride was used  
256 to relate soil water concentrations of chloride,  $\text{Cl}^-$ , to  $\sigma_w$ .

### 257 **3.4. Inversion of time-lapse EMI $\sigma_a$ data**

258 Time-lapse  $\sigma_a$  data obtained during the experiments were inverted using a modified inversion  
259 algorithm proposed by Monteiro Santos et al. (2004) to obtain  $\sigma_b$  distribution in time. The aim of  
260 the inversion is to minimize the penalty function that consists of a combination between the  
261 observations' misfit and the model roughness (Farzamian et al., 2019b). The earth model used  
262 in the inversion process consists of a set of 1D models distributed according to the number of time-  
263 lapse measurements. All the models have the same number of layers (i.e. 7) whose thickness is  
264 kept constant. The selected [thickness-depths](#) of layers ~~is~~ [are](#) 10, 20, 30, 40, 55, 75 and 180 cm. The  
265 number and thickness of layers were selected based on several factors including the number of  $\sigma_a$

266 measurements (i.e., 6), effective depth range of HCP and VCP modes (i.e., 5 of 6 measurements  
 267 have an effective depth of less than 1m), and site specifications (i.e., the large variability of  
 268 conductivity of the soil profile over a resistive bedrock). The parameters of each model are  
 269 spatially and temporally constrained using their neighbours through smooth conditions. The  
 270 forward modelling is solved based on the full solution of the Maxwell equations (Kaufman and  
 271 Keller, 1983) to calculate the  $\sigma_a$  responses of the model. The inversion algorithm is Occam-  
 272 regularization and the objective function was developed based on Sasaki, (2001). Therefore, the  
 273 [corrections-update](#) of the parameters, in an iterative process are calculated solving the system:

$$274 \quad [(J^T J + \eta C^T C)] \delta p = J^T b \quad (2)$$

275 where  $\delta p$  is the vector containing the corrections applied to the parameters (logarithm of  
 276 block conductivities,  $p_j$ ) of an initial model,  $b$  is the vector of the differences between the logarithm  
 277 of the observed and calculated  $\sigma_a$  [ $b_i = \ln(\sigma_a^o/\sigma_a^c)_i$ ],  $J$  is the Jacobian matrix whose elements are  
 278 given by  $(\sigma_j/\sigma_{ai}^c) (\partial\sigma_{ai}^c/\partial\sigma_j)$ , the superscript T denotes the transpose operation, and  $\eta$  is a Lagrange  
 279 multiplier that controls the amplitude of the parameter corrections and whose best value is  
 280 determined empirically. The elements of matrix  $C$  are the coefficients of the values of the  
 281 roughness of each 1D model, which is defined in terms of the two neighbour's parameters and the  
 282 [constraint](#) between the parameters of the different models on time. In this regard and in [our the](#)  
 283 temporal 1D experiment, each cell is constrained spatially by its vertical neighbours, while the  
 284 temporal constraints are imposed using its lateral neighbours. An iterative process allows the final  
 285 models to be obtained, with their response fitting the data set in a least-square sense. In terms of  
 286  $\eta$ , generally, large values will produce smooth inversion results with smoother spatial and temporal  
 287 variations.

288 We performed several syntenic tests to determine how well the proposed inversion algorithm  
289 can predict spatiotemporal variability of  $\sigma_b$  and to fine-tune the regularization parameters. The  
290 syntenic scenarios were selected based on spatiotemporal variability of  $\sigma_a$  in the HCP and VCP  
291 modes, the site specification (e.g. shallow bedrock) and the expected evolution of conductive zone  
292 due to water and saline water infiltrations.

### 293 **3.5. Numerical simulation of water flow and chloride transport in soil**

294 The water and the chloride propagation monitored during the experiments were simulated by  
295 using the HYDRUS-1D model (Šimůnek et al., 1998b). HYDRUS-1D simulates water flow and  
296 solute transport by solving the Richards equation and the Advection-Dispersion equation,  
297 respectively.

298 Richards equation can be written for one-dimensional, unsaturated, non-steady state flow of  
299 water in the vertical direction as follows:

$$300 \quad C_w(\theta) \frac{\partial h}{\partial t} = \frac{\partial}{\partial z} \left[ K(h) \frac{\partial h}{\partial z} + K(h) \right] \quad (3)$$

301 where  $C_w(\theta)$ , the water capacity, is the slope of the water retention curve,  $\theta$  is the volumetric water  
302 content [ $L^3L^{-3}$ ],  $h$  is the soil water pressure head [L],  $K(h)$  is the unsaturated hydraulic conductivity  
303 [ $LT^{-1}$ ].

304 The Advection-Dispersion equation governing the transport of a single non-reactive and non-  
305 adsorbed (a tracer, chloride in ~~our~~[this](#) case) ion in the soil can be written as:

$$306 \quad \frac{\partial(\theta C)}{\partial t} = \frac{\partial}{\partial z} \left[ \theta D \frac{\partial C}{\partial z} - qC \right] \quad (4)$$

307 where  $q$  is the darcian flux,  $C$  is the solute concentration in the liquid phase [ $ML^{-3}$ ],  $D$  ( $L^2T^{-1}$ ) is  
308 the effective dispersion coefficient, which can be assumed to come from a combination of the

309 molecular diffusion coefficient,  $D_{\text{diff}}$  ( $\text{L}^2\text{T}^{-1}$ ) and the hydrodynamic dispersion coefficient,  $D_{\text{dis}}$   
310 ( $\text{L}^2\text{T}^{-1}$ ):

$$311 \quad D = D_{\text{diff}} + D_{\text{dis}} \quad (5)$$

312 where hydrodynamic dispersion is the mixing or spreading of the solute during transport due to  
313 differences in velocities within a pore and between pores. The dispersion coefficient can be related  
314 to the average pore water velocity  $v=q/\theta$  through:

$$315 \quad D = \lambda v \quad (6)$$

316 where  $\lambda$  [L] is the dispersivity, a characteristic property of the porous medium. To solve the  
317 Richards equation (Eq. 3), the water retention function,  $\theta(h)$ , and the hydraulic conductivity  
318 function,  $K(h)$ , must be defined. In this paper we adopted the van Genuchten-Mualem model (vG-  
319 M), (van Genuchten, 1980):

$$320 \quad S_e = [1 + (\alpha|h|)^n]^{-m} \quad (7)$$

$$321 \quad K(h) = K_s S_e^\tau \left[1 - (1 - S_e^{1/m})^m\right]^2 \quad (8)$$

322 In Eqs. 7 and 8,  $S_e = \frac{(\theta - \theta_r)}{(\theta_s - \theta_r)}$  is the effective water saturation,  $\theta_s$  the saturated water content,  $\theta_r$  the  
323 residual water content,  $\alpha$ ,  $n$  and  $m$  are fitting parameters with  $m$  taken as  $m=1-1/n$ ,  $K_s$  is the  
324 saturated hydraulic conductivity and  $\tau$  is the pore-connectivity parameter.

325

### 326 **3.6. Inverse estimation of soil hydraulic and solute transport parameters**

327 The obtained EMI-based spatiotemporal distribution of  $\sigma_b$  during the 1<sup>st</sup> experiment was  
328 converted to the  $\theta$  distribution in order to estimate the temporal evolution of  $\theta$  during the



329 infiltration process. These water content data were then used in an optimization procedure by using  
330 the HYDRUS-1D model, in order to estimate the hydraulic properties of the different horizons in  
331 the soil profile. The simulations were carried out by using the actual top boundary flux conditions  
332 during the experiment, including the irrigation events. For the bottom boundary, free drainage was  
333 considered. A simulation domain of 150 cm depth was considered. The same procedure was  
334 repeated using the direct measurements of  $\theta$  and  $h$  inferred from TDR and tensiometers,  
335 respectively, in order to obtain independent hydraulic parameters (TDR-based estimation) to be  
336 compared to those inferred from EMI. A three-layer soil profile (0-25; 25-70; 70-150 cm),  
337 reflecting the actual pedological layering (i.e. Ap, Bw, and bedrock) was used in all simulations.  
338 In terms of the initial condition, a hydrostatic distribution of the pressure heads,  $h$ , was considered  
339 for the TDR-based simulations. On the other hand, the water content distribution, inferred from  
340 the first EMI survey (before irrigation) was considered for the EMI-based simulation.

341 As for the solute transport experiment, a HYDRUS-1D simulation was carried out with the  
342 EMI-based hydraulic properties obtained from the 1<sup>st</sup> experiment to simulate the water content  
343 distributions in correspondence with the EMI measurement times. The simulations of water  
344 infiltration and solute transport in the 2<sup>nd</sup> experiment were carried out by using the top boundary  
345 fluxes conditions applied during the 2<sup>nd</sup> experiment along with the same simulation domain, three-  
346 layer soil profile, and the bottom boundary and equilibrium initial conditions described above.  
347 Thus, for each monitoring time, we had available the  $\sigma_b$  distributions obtained from the EMI and  
348 the  $\theta$  distributions coming from the HYDRUS-1D simulations. These distributions allowed us to  
349 estimate as many  $\sigma_w$  (and thus  $C$ ) distributions by using the  $\theta$ - $\sigma_b$ - $\sigma_w$  relationship obtained in the  
350 laboratory. These  $C$  distributions were used in a new HYDRUS-1D simulation to estimate the

351 longitudinal dispersivity of the investigated soil. The simulated concentrations, with the optimized  
352 dispersivity,  $\lambda$ , were compared to those obtained from the TDR and tensiometer data.

353

## 354 **4. RESULTS AND DISCUSSION**

### 355 **4.1. Water infiltration – 1<sup>st</sup> experiment**

#### 356 *4.1.1. Time-lapse $\sigma_a$ data and estimation of $\sigma_b$ distribution*

357 Figure 3 shows the  $\sigma_a$  values observed during the water infiltration experiment. Both VCP  
358 and HCP modes show a relatively similar pattern of  $\sigma_a$  values with  $\rho32$  and  $\rho118$  being the highest  
359 and lowest respectively. HCP mode shows higher values compared to the VCP mode in the same  
360 receivers. This pattern of  $\sigma_a$  distribution suggests the presence of a conductive zone over a resistive  
361 zone which is expected in this experiment as a result of the waterfront being infiltrated into the  
362 soil profile and the presence of a resistive bedrock. In terms of temporal  $\sigma_a$  variabilities, the  $\sigma_a$   
363 increases consistently in both VCP and HCP modes during the first three hours of the experiment.  
364 Afterward,  $\sigma_a$  did not change significantly toward the end of the experiment. The range of  $\sigma_a$   
365 variations is relatively small in both VCP and HCP modes with the former in the 10-30 mS m<sup>-1</sup>  
366 range and the latter in the 10-50 mS m<sup>-1</sup> range.

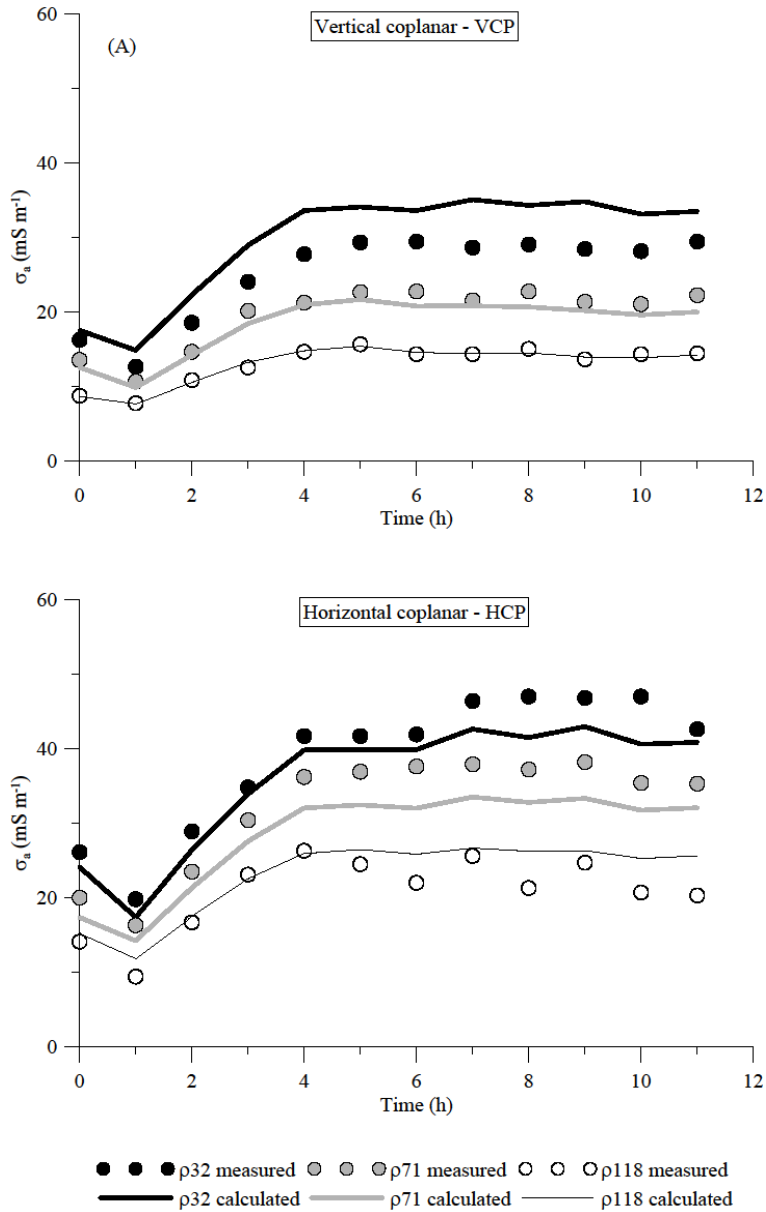
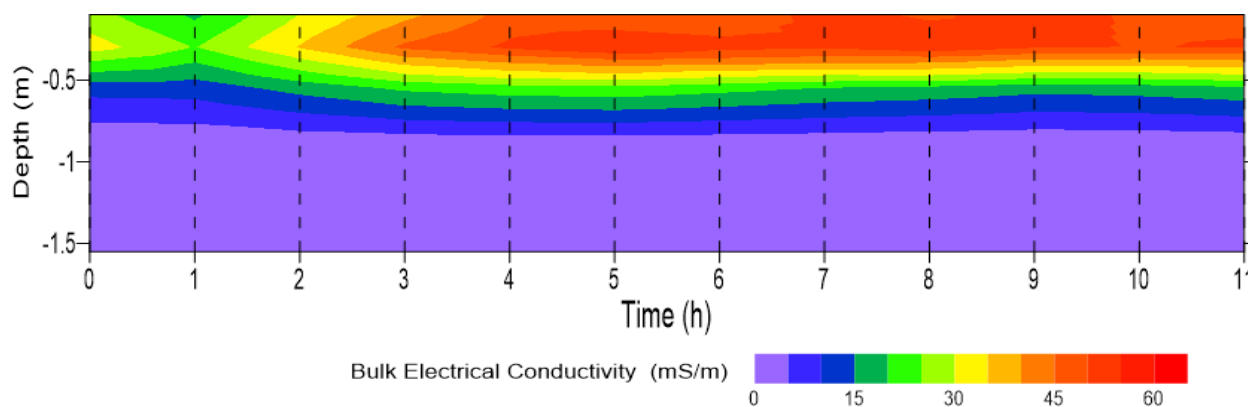


Figure 3:  $\sigma_a$  values observed during the water infiltration experiment. (A) VCP, (B) HCP. The symbols represent the measured data whereas the lines represent the values calculated after the inversion.

367 Prior to the inversion of  $\sigma_a$  data we fine-tuned the regularization parameter,  $\eta$ , as discussed  
 368 in 3.4. the results of several synthetic tests (not shown here) suggest that a value of  $\eta$  between 1 to

369 5 provides a better result in resolving the spatio-temporal  $\sigma_b$  distributions in both experiments.  
 370 Figure 4 depicts the time-lapse  $\sigma_b$  modelling results of  $\sigma_a$  shown in Fig. 3. The model shows clearly  
 371 the evolution of the conductive zone into the soil profile shortly after the irrigation started as  
 372 expected from the  $\sigma_a$  data. The resistive zone beneath a conductive zone corresponds to the bedrock  
 373 layer in the experimental plot. The  $\sigma_b$  of the resistive zone remains below  $5 \text{ mS m}^{-1}$  and does not  
 374 vary significantly during the experiment, while, in contrast, the  $\sigma_b$  of the upper layers increased  
 375 significantly from an average of  $20 \text{ mS m}^{-1}$  at the beginning of the experiment to more than  $50 \text{ mS}$   
 376  $\text{m}^{-1}$  after the 5<sup>th</sup> irrigation. The conductivity of this zone does not increase largely since then,  
 377 suggesting that the upper soil is fairly saturated after the 5<sup>th</sup> irrigation. The calculated response of  
 378 this model was shown in Fig. 3. There is a fairly good agreement between  $\sigma_a$  measurements and  
 379 model response, however, a slight shift can be noticed in the  $\rho_{32}$ - VCP mode and  $\rho_{71}$ - HCP mode  
 380 between data and model response. This shift can be due to several reasons such as i) the  
 381 instrumental ~~shift of one or more channels~~drift of the EMI sensor, ii) the large spatiotemporal  
 382 variability of soil electrical conductivity in this experiment as well as smoothness constraint  
 383 performed in the inversion process to stabilize the inversion process which make it difficult to  
 384 resolve the sharp changes, and iii) the choice of initial model.



385  
 386 Figure 4. Time evolution of bulk electrical conductivity ( $\sigma_b$ ) distribution with depth during the  
 387 water infiltration experiment.

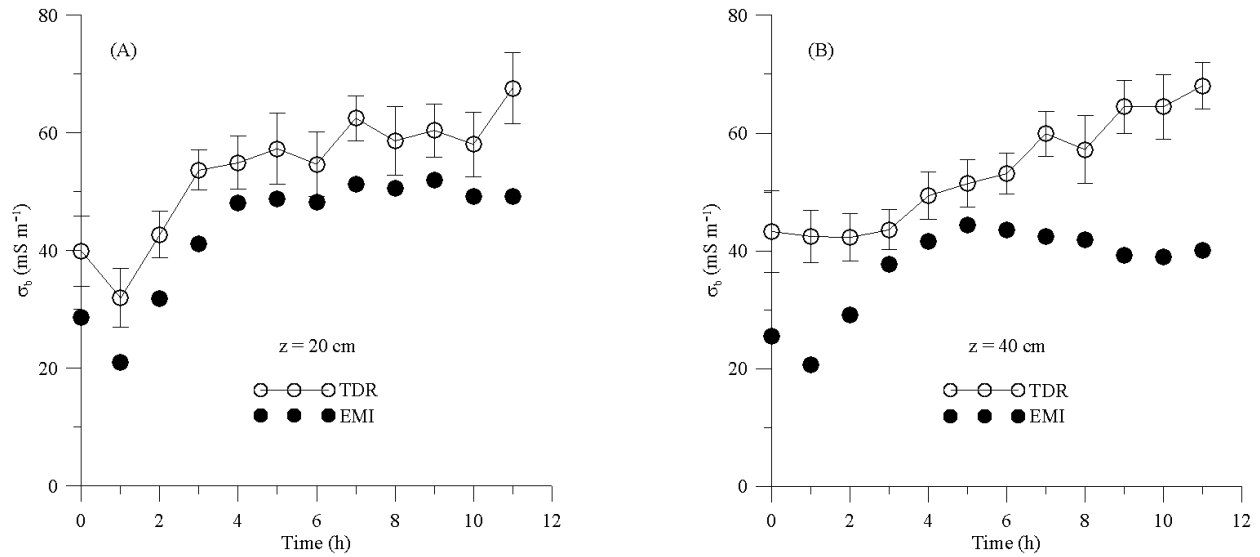
#### 4.1.2. Comparison between TDR-based and EMI-based $\sigma_b$ and $\theta$ distributions

Figure 5 shows the temporal  $\sigma_b$  changes inferred from TDR and EMI observations at two depths, 20 and 40 cm. As reported by some authors (e.g. Coppola et al., 2016; Dragonetti et al., 2018), both techniques provide  $\sigma_b$  estimations but a direct comparison between  $\sigma_b$  by TDR and EMI is not straightforward due to different observation volumes of the two sensors. ~~As argued by Coppola et al. (2016), “because of its relatively small observation volume, a TDR probe provides a quasi-point like measurements and do not integrate the small scale variability (in soil water content, solute concentrations, etc.) induced by natural soil heterogeneity. By contrast, EMI data necessarily overrule the small-scale heterogeneities seen by TDR probes as they investigate a much larger volume”.~~ However, this comparison can be used as a means to investigate the consistency of the  $\sigma_b$  trends and to provide an insight into the uncertainty associated with the EMI survey and inversion process in resolving the water infiltration process into the soil profile. Note that the average of TDR measurements in four corners at depths of 20 and 40 cm were considered both in this comparison and in the inversion procedure. The average values and the standard deviation of TDR measurements were presented in Fig. 5.

Focusing on the  $\sigma_b$  series inferred from both TDR observations and EMI inversion, a similar time pattern of  $\sigma_b$  variability is evident, but in general, the EMI model underestimates the  $\sigma_b$  obtained by TDR. A better agreement was observed at 20 cm in terms of both absolute  $\sigma_b$  values and trend ( $r=0.94$ ; Mean Error= $10.1 \text{ mS m}^{-1}$ ). In contrast, at 40 cm, the mismatch between TDR observations and EMI inversions becomes larger at the end of the experiment. The EMI  $\sigma_b$  values – especially at 40 cm depth – remain rather invariant in the last part of the infiltration experiment. The general outcome that for both layers the EMI  $\sigma_b$  values underestimate the TDR  $\sigma_b$  measurements has been frequently found in the literature (e.g. von Hebel et al., 2014; Coppola et

411 al., 2015; Dragonetti et al., 2018; Visconti and [de Paz, 2021](#)). ~~von Hebel et al. (2014) also found a~~  
412 ~~similar behaviour when comparing their EMI results with ERT surveys. In that case, the  $\sigma_a$  values~~  
413 ~~measured by EMI systematically underestimated the  $\sigma_a$  generated by applying EMI forward~~  
414 ~~modelling to the  $\sigma_b$  distribution retrieved from the ERT surveys.~~ Furthermore, TDR measurements  
415 show a low local variability, as depicted in Fig. 5 by the error bars reporting the standard deviation  
416 of the  $\sigma_b$  as measured by the four TDR probes.

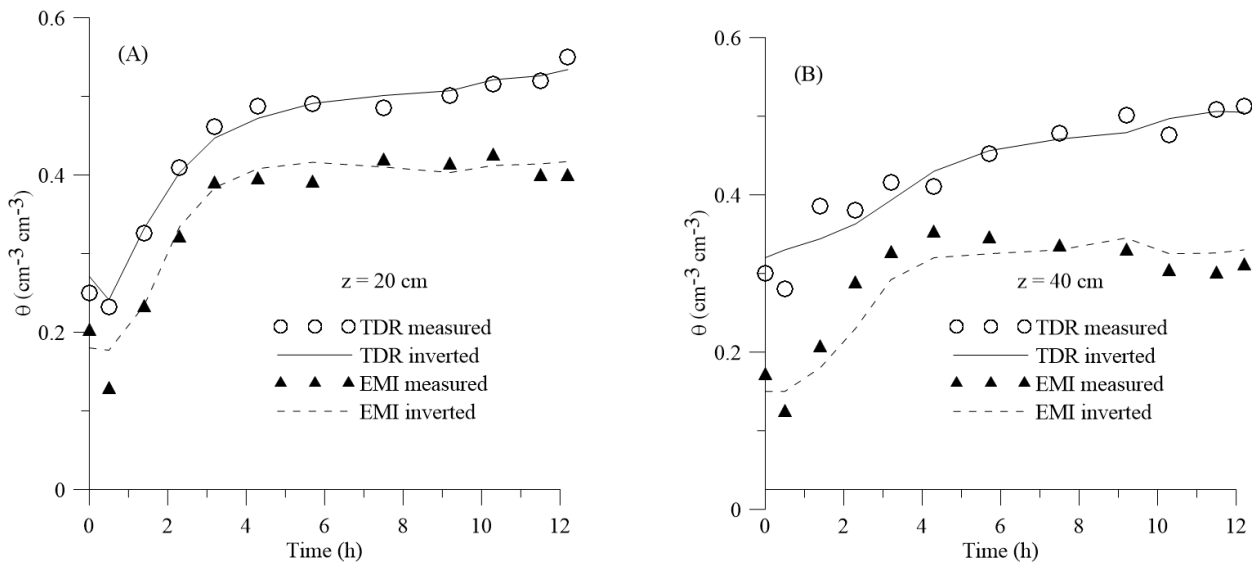
417         Figure 6 shows the evolution of  $\theta$  at the same two depths, 20 and 40 cm as observed by  
418 TDR and EMI sensors. TDR provides the direct in-situ measurement of  $\theta$ . In contrast in order to  
419 estimate  $\theta$  from EMI observation,  $\sigma_b$  values extracted at these depths (Fig. 4) were converted to  $\theta$   
420 by the calibration performed in the laboratory, as detailed in [Farzamian et al., \(2021\)](#). A rapid  
421 increase of  $\theta$  is visible shortly after injection in both EMI-based and TDR-based measurements.  
422 The EMI-based  $\theta$  estimation is able to detect the similar water content evolution (similar water  
423 content differences over time) observed by TDR measurements but at a different water content  
424 level. Specifically, EMI water contents were lower than the TDR ones but the two series showed  
425 a quasi-parallel evolution at 20 cm depth ( $r=0.98$ ; Mean Error= $0.09 \text{ cm}^3 \text{ cm}^{-3}$ ), while diverging for  
426 longer times at 40 cm depth ( $r=0.60$ ; Mean Error= $0.17 \text{ cm}^3 \text{ cm}^{-3}$ ).  
427



428

429 Figure 5.  $\sigma_b$  evolution estimated from the TDR and EMI measurements at 20 cm (A) and 40 cm  
 430 (B) depths. The vertical bars represent the standard deviation of the measurements obtained by the  
 431 four TDR sensors.

432



433

434 Figure 6. Evolution of  $\theta$  measured by TDR (circles) and estimated from EMI measurements  
 435 (triangles) at 20 cm (A) and 40 cm (B) depths. Continuous lines for TDR and dashed lines for EMI  
 436 refer to the estimation obtained by the inversion procedure of the water infiltration process (see  
 437 Sect. 4.1.3 below).

438

439 4.1.3. *Estimation of hydraulic properties*

440 In order to estimate hydraulic properties parameters, an inversion procedure was carried  
441 out applying HYDRUS-1D. The first set of hydraulic parameters was obtained by using the soil  
442 water contents measured by TDR and the pressure heads measured by tensiometers as measured  
443 data in the objective function for the optimization procedure (TDR-based). The second set of  
444 hydraulic parameters was obtained by using the soil water contents estimated by EMI  
445 measurements as measured data (EMI-based). The inversion simulations were carried out by fixing  
446  $\theta_r=0$  and  $\tau=0.5$ , while  $\theta_s$ ,  $\alpha$ ,  $n$  and  $K_s$  were optimized for both the Ap and the Bw layers. The  
447 hydraulic properties of the bedrock were already known and fixed to  $\theta_r=0.068$ ,  $\theta_s=0.354$ ,  $\alpha=0.055$ ,  
448  $n=3.67$ ,  $\tau=0.5$  and  $K_s=19.02$  according to Caputo et al. (2010; 2015). We want to stress here that  
449 an a-priori characterization of the bedrock layer is not essential and the proposed procedure holds  
450 independently on the presence of bedrock. We could have treated the bedrock layer as any other  
451 layer in the soil profile, but inserting TDR probes and tensiometers into bedrock presents  
452 difficulties. Therefore, we decided to fix the bedrock parameters to the values already available  
453 from independent measurements. In different soils with either deeper or absent bedrock, we could  
454 have inserted TDR probes into deeper layers of the profile and applied the procedure to any of  
455 them.

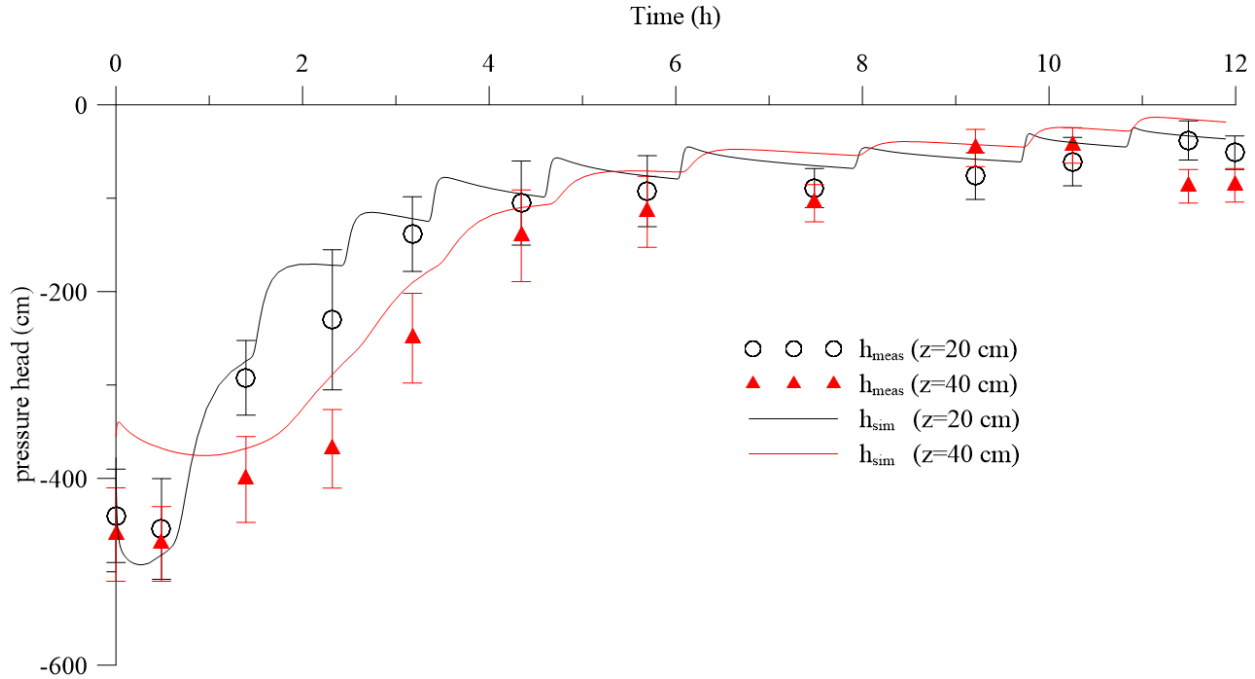
456 In the inversion procedure, the parameters were determined separately for each horizon of  
457 the profile ([Abbaspour et al., 1999](#)). First, the parameters for the topsoil were estimated and these  
458 parameters were then treated as known for the second layer estimation. [Despite the water content  
459 development in one layer is not independent on the hydraulic properties of the other layers when  
460 long-time evolution is considered, in the case of a relatively short infiltration event as used here,  
461 this approach makes parameter estimation of multi-layered profiles feasible. According to](#)



462 ~~Abbaspour et al. (1999), this approach makes parameter estimation of multi-layered profiles more~~  
463 ~~feasible and accurate.~~ It should be noted that in the case of the TDR-based estimations,  
464 optimization involved both measured water contents and pressure head data, whereas the EMI-  
465 based estimations only involved “measured” water contents.

466 Figure 6 reports a comparison between water contents measured (symbols) and estimated  
467 (lines) by the inversion procedure. The  $\theta$  evolution was properly estimated at 20 cm depth in both  
468 approaches. It is worth noting here that, despite the differences in the absolute value of the water  
469 contents, a clear parallel behaviour of the two curves was observed, suggesting similar water  
470 content changes over time. A lower agreement was obtained at 40 cm but still reproduced similar  
471 water content changes over time. This is a crucial point in this paper, as the parallel behaviour of  
472 the water content evolution will explain the similar shape of hydraulic properties we found for the  
473 TDR and EMI-based estimations (see below, Figure 8).

474 ~~as it is the main reason for the shape of the hydraulic properties we found for the TDR and~~  
475 ~~EMI-based estimations.~~



477

478 Figure 7. Evolution of pressure head at 20 and 40 cm depth measured by tensiometers (symbols)  
 479 and estimated by the inversion procedure (lines) of the water infiltration process. The vertical bars  
 480 represent the standard deviation of the measurements obtained by the four tensiometers.

481

482 Similarly, in Fig. 7 the measured (points) and estimated (lines) values of pressure heads  
 483 are shown. The simulated values of pressure head well follow the measured one ( $r=0.950$  at 20 cm  
 484 and  $r=0.986$  at 40 cm depth). Furthermore, the error bars, reporting the standard deviation of the  
 485 pressure head as measured by the four tensiometers, overlap when the profile is wet (i.e. after the  
 486 6th irrigation) and separate during the wetting process.

487 Table 1 reports the parameters of the hydraulic functions, estimated for the first two  
 488 horizons and Fig. 8 reports the water retention curves and the hydraulic conductivity curves  
 489 corresponding to the parameters shown in table 1 for a better comparison between TDR-based and  
 490 EMI-based hydraulic properties assessment. [Compared to the Ap horizon, higher  \$K\_s\$  and lower  \$n\$](#)

491 [values were found for the Bw horizon. This may be explained by considering that tillage in the Ap](#)  
 492 [horizon changes the geometry of the porous system, by reducing the structural pores, responsible](#)  
 493 [of the lower  \$K\_s\$  for Ap, and increasing the textural pores, explaining the higher  \$n\$  value for Ap.](#)

494 Note in the table the high values of  $n$  and  $K_s$  for the bedrock, which indicate a high conductive  
 495 porous medium. It is possible to explain this by considering that the bedrock is fractured  
 496 calcareous, which, contrary to expectation, does not impede water flow.

497

498 Table 1. vG-M Hydraulic parameters (Eqs. 7 and 8) and dispersivity,  $\lambda$  (Eq. 6) as estimated for Ap  
 499 and Bw horizons, and fixed for the bedrock layer.

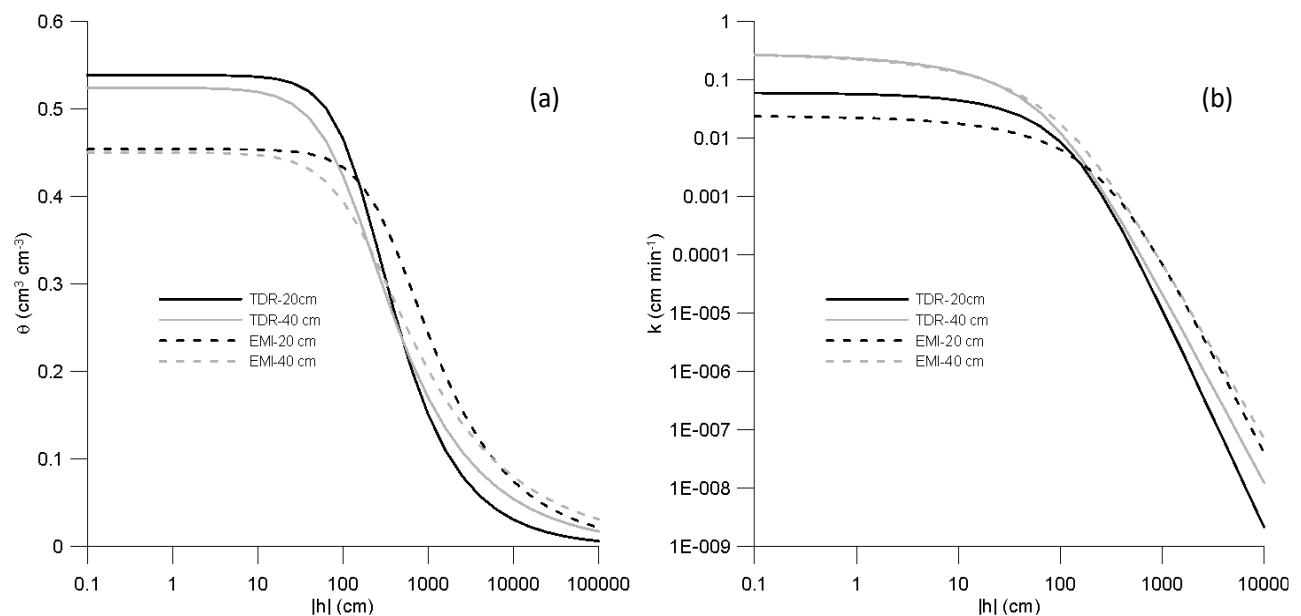
Soil hydraulic and transport parameters*		Ap		Bw		Bedrock
		TDR-based	EMI-based	TDR-based	EMI-based	Fixed a-priori
$\theta_s$	[cm <sup>3</sup> cm <sup>-3</sup> ]	0.54	0.45	0.52	0.45	0.354
$\alpha$	[cm <sup>-1</sup> ]	0.006	0.003	0.009	0.007	0.055
$n$	[-]	1.70	1.54	1.50	1.41	3.67
$k_s$	[cm min <sup>-1</sup> ]	0.06	0.02	0.28	0.29	19
$\lambda$	[cm]	10	12	0.5	0.8	30

500 \* For all horizons  $\theta_r=0$  and  $\tau=0.5$ .

501 As for water retention, the TDR and EMI water retention curves showed similar shapes but  
 502 with slightly different saturated water contents. As discussed earlier, the lower saturated water  
 503 content is not surprising for the EMI-based estimation due to the overall underestimation of water  
 504 content. The two curves almost overlapped once scaling the EMI curve by the ratio of the saturated  
 505 water contents. Obviously, this result is consistent with the underestimation of EMI-based  $\theta$   
 506 distributions as shown in Fig. 6.

507 As for the hydraulic conductivity, TDR-based and EMI-based hydraulic conductivity  
 508 curves at both 20 and 40 cm appear to almost overlap, with similar saturated hydraulic conductivity

509 and curve shape. This result is expected because the shape of hydraulic conductivity curve is  
 510 mainly a function of explained by the variation of  $\theta$  and not the absolute value of  $\theta$  itself. It is  
 511 worth mentioning that the same top boundary flux and different water contents in the soil profile  
 512 provided similar EMI-based and TDR-based hydraulic conductivity. These conditions led to two  
 513 different water flow processes, with simulations predicting higher water stored in the soil profile  
 514 and lower downward fluxes (data not shown) when TDR-based results are compared to the EMI-  
 515 based results.



516

517 Figure 8. Soil water retention (A) and unsaturated hydraulic conductivity (B) curves, estimated  
 518 from the TDR and EMI measurements at 20 cm and 40 cm depths.

519

## 520 4.2. Solute Infiltration – 2<sup>nd</sup> Experiment

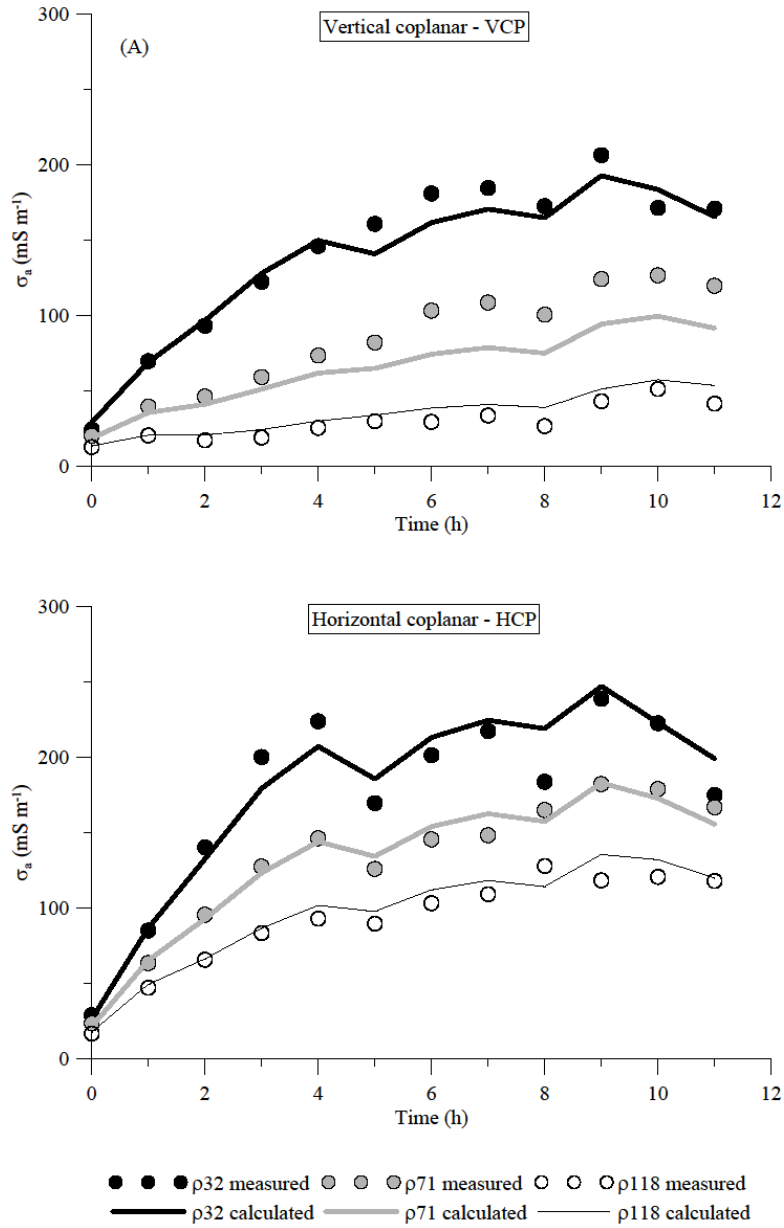
### 521 4.2.1. Time-lapse $\sigma_a$ data and estimation of $\sigma_b$ distribution

522 Figure 9 shows the  $\sigma_a$  data collected during the solute infiltration experiment. Again, as for  
 523 the 1<sup>st</sup> experiment, both VCP and HCP modes show a relatively similar pattern of  $\sigma_a$  values with  
 524  $\rho_{32}$  and  $\rho_{118}$  being the highest and lowest respectively. HCP mode shows higher values on

525 average compared to the VCP mode. Similarly, to the water infiltration experiment,  $\sigma_a$  increases  
526 consistently during the first three hours of the experiment, then it does not change significantly or  
527 consistently until the end of the experiment. Much higher ranges of  $\sigma_a$  variations were measured  
528 in both VCP and HCP configurations, with  $\sigma_a$  values ranging in 20-200 and 50-250  $\text{mS m}^{-1}$   
529 respectively.

530 Figure 10 depicts the  $\sigma_b$  evolution for the 2<sup>nd</sup> experiment, obtained by time-lapse inversion  
531 of  $\sigma_a$  data.  $\sigma_a$  measurements and model response agrees fairly as shown in Fig. 9, however a slight  
532 shift can be noticed in the p71- VCP mode between data and model response. The results show the  
533 rapid evolution of the conductive zone to the soil profile shortly after the irrigation started. In  
534 comparison to the obtained  $\sigma_b$  in the 1<sup>st</sup> experiment, the results reveal significantly higher soil  
535 conductivity in topsoil but a much slower evolution. The conductivity of the top layer exceeds 300  
536  $\text{mS m}^{-1}$  shortly after the irrigation. The higher topsoil conductivity results from injection of high-  
537 saline water (about 15  $\text{dS m}^{-1}$ ) that dramatically increases soil conductivity whereas the smaller  
538 evolution of the conductive zone is caused by significantly slower concentration propagation into  
539 the soil profile.

540

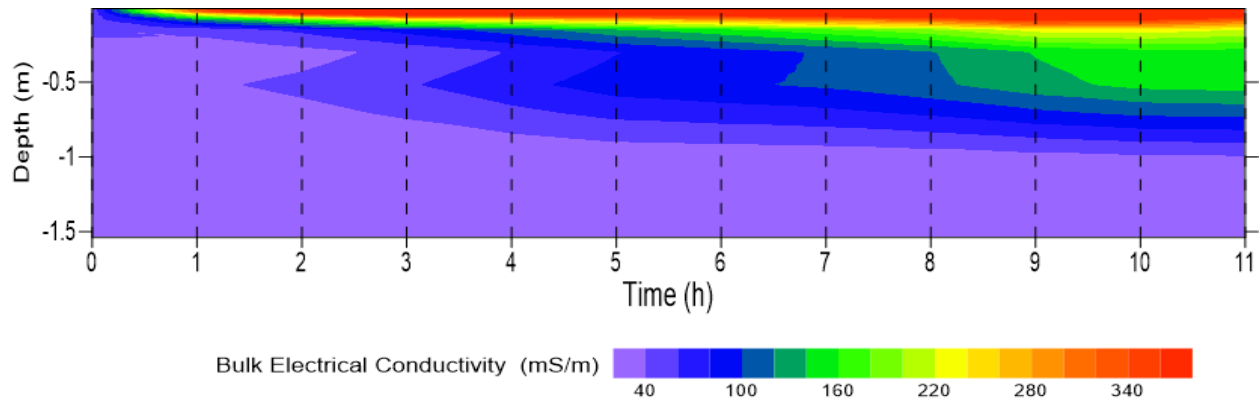


541

542 Figure 9:  $\sigma_a$  values observed during the solute infiltration experiment. (A) VCP, (B) HCP. The  
 543 symbols represent the measured data whereas the lines represent the values calculated after the  
 544 inversion.

545

546



547

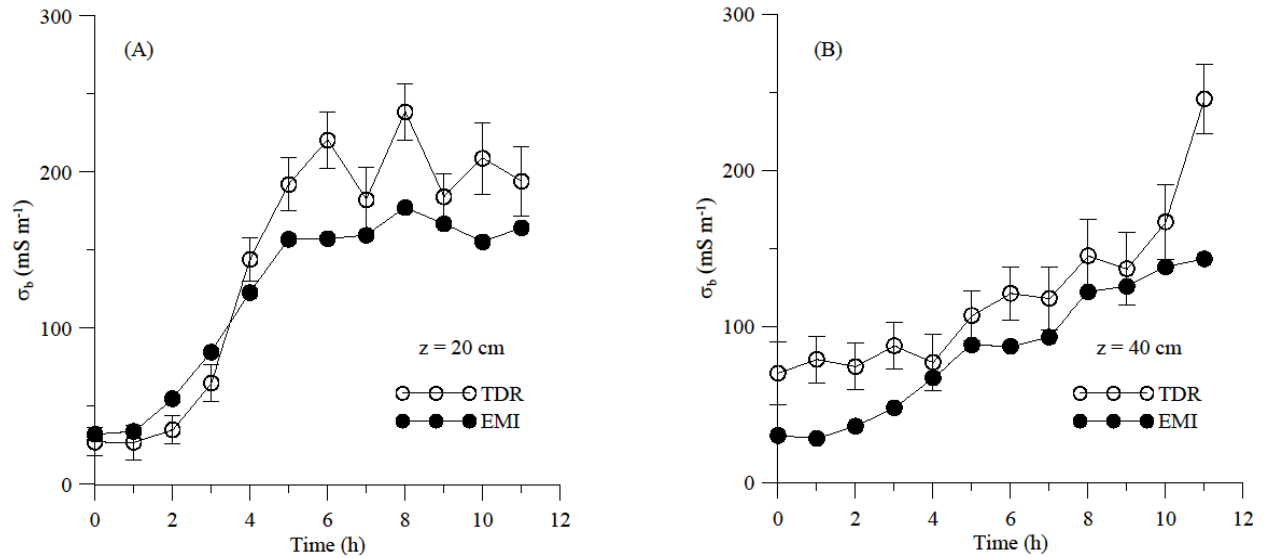
548 Figure 10. Time evolution of bulk electrical conductivity ( $\sigma_b$ ) during the solute infiltration  
 549 experiment.

550

#### 551 4.2.2. Comparison between TDR-based and EMI-based $\sigma_b$ and $[Cl^-]$ distributions

552

553 Figure 11 shows the comparison between the  $\sigma_b$  values obtained by the TDR measurements  
 554 and those obtained from the EMI inversion (Fig. 10) during the 2<sup>nd</sup> experiment. As discussed  
 555 above, this comparison is to provide an insight into the potential of the EMI survey and inversion  
 556 process in monitoring a solute transport experiment into a soil profile. The comparison shows a  
 557 similar time pattern of  $\sigma_b$  variability, but in general the EMI model underestimates the  $\sigma_b$  obtained  
 558 by TDR. The results of this comparison agree with the 1<sup>st</sup> experiment where, again, the EMI-based  
 559  $\sigma_b$  are lower compared to those measured by the TDR. In contrast to the 1<sup>st</sup> experiment, the  
 560 differences between the two techniques and in terms of the absolute  $\sigma_b$  values are of minor concern.  
 561 This could be due to the larger conductivity contrast that tracer introduced into the soil profile in  
 562 the 2<sup>nd</sup> experiment which became easier to detect by using the EMI sensor. On the other hand, the  
 563 TDR probes show more fluctuations in  $\sigma_b$  measurements, especially at 20 cm. We attribute these  
 564 fluctuations to the smaller volume of investigation of the TDR probes which are very sensitive to  
 565 the process taking place very close to the probe and, therefore, strongly influenced by small-scale  
 heterogeneities.



566

567 Figure 11.  $\sigma_b$  evolution estimated by TDR and EMI measurements at 20 cm (A) and 40 cm (B)  
 568 depth.

569

570 The next step in the procedure allows us to determine the distribution of  $\text{Cl}^-$  concentrations  
 571 by EMI sensors (Sect. 4.2.3.) used for estimating the longitudinal dispersivity of the two soil layers  
 572 investigated. For the sake of comparison, TDR-based  $[\text{Cl}^-]$  distributions were obtained directly in  
 573 the field from a direct measurement of the  ~~$\sigma_b$  impedance  $Z$  along the TDR transmission line~~  
 574 ~~embedded in the soil~~. As for the EMI-based  $\text{Cl}^-$  concentrations, a forward HYDRUS-1D simulation  
 575 was carried out using the EMI-based hydraulic properties obtained from the 1<sup>st</sup> experiment and  
 576 reported in Table 1 to estimate the water content distributions in correspondence with the EMI  
 577 measurement times of the 2<sup>nd</sup> experiment. These water contents, combined with the available  $\sigma_b$   
 578 distribution obtained from the EMI inversion, allowed us to obtain the  $\sigma_w$  distributions (through  
 579 the  $\theta$ - $\sigma_b$ - $\sigma_w$  calibration relationship) for both depths and, consequently, the  $[\text{Cl}^-]$  distributions.

580



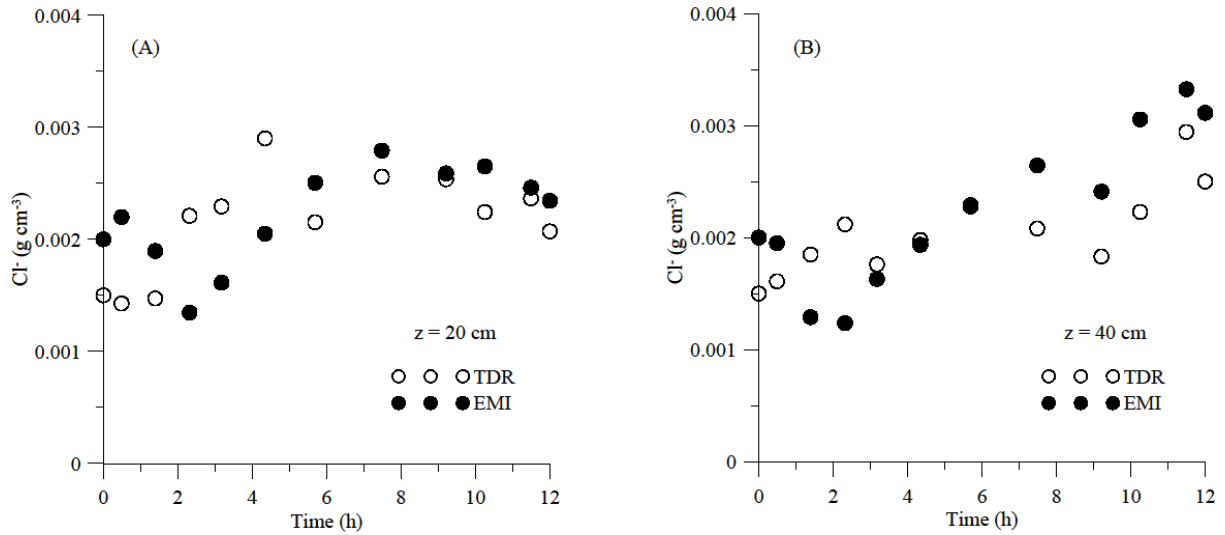


Figure 12.  $[\text{Cl}^-]$  distributions inferred from EMI and TDR measurements, at 20 (A) and 40 (B) cm depth.

581 Figure 12 shows the  $[\text{Cl}^-]$  distributions inferred from EMI compared to the TDR  
 582 measurements. The comparison suggests a good agreement between the two time-series. The EMI-  
 583 based concentrations underestimate – on average – the TDR-based ones by 4% and by 7% at 20  
 584 cm and 40 cm depths, respectively. The time evolution of the two data series reveals marked  
 585 differences, as shown by the very different correlation:  $r = -0.04$  for the 20 cm depth and  $r = 0.70$   
 586 for the 40 cm depth. The difference between the two data series at both depths can be mostly  
 587 explained by the differences between  $\sigma_b$  distributions shown in Fig. 11. Additionally, another point  
 588 of difference may arise from the assumption that the water content distribution obtained from the  
 589 HYDRUS-1D simulation can be used as a substitute for the water content measurements, in order  
 590 to obtain  $[\text{Cl}^-]$  from the EMI readings.

#### 591 4.2.3. Estimation of longitudinal dispersivity

592 Inverse HYDRUS-1D simulations were conducted using concentration data provided by both  
 593 the TDR and EMI results, in order to estimate the longitudinal dispersivity for both Ap and Bw  
 594 horizons. The results are reported in the last row of Table 1. TDR-based and EMI-based procedures

595 provide similar values of  $\lambda$ . Specifically, for the Ap horizon, the obtained values agree with those  
596 frequently found in the literature for either large columns or field-measured dispersivity (e.g.  
597 Vanderborght and Vereecken, 2007; Coppola et al., 2011). The TDR and EMI-based estimation  
598 of dispersivity for the Bw horizon shows one order of magnitude lower values compared to the Ap  
599 horizon. These values are more consistent with values measured in the laboratory (Coppola et al.,  
600 2019). For column scale (undisturbed soil monoliths with a length > 30 cm), Vanderborght and  
601 Vereecken (2007) found values in the order of 10 cm. The same values were found by Coppola et  
602 al. (2011) at both plot and transect scales. Note in the Table 1 the high value of dispersivity used  
603 for the bedrock layer. This is consistent with the nature of the bedrock, which, as mentioned, is a  
604 fractured calcareous and highly conductive rock, which may well explain high dispersivity values.

605

## 606 **5. FURTHER DISCUSSION ON THREE KEY POINTS OF THE PROPOSED** 607 **APPROACH**

608 Following, ~~our~~the discussion will focus on three major aspects of this research in terms of the  
609 choice of approach (uncoupled vs coupled), the suitability of EMI as a replacement for invasive  
610 sensors, and EMI-related sources of uncertainty.

### 611 **5.1. Uncoupled vs Coupled approach**

612 In hydro-geophysical studies there is an ample debate on this issue. Camporese et al. (2015),  
613 stated in their conclusions: “the relative merit of the coupled approach versus the uncoupled one  
614 cannot be assumed a priori and should be assessed case by case. As the information content of the  
615 geophysical data remains the same in both the coupled and uncoupled methods, the main difference  
616 is the approach taken in order to complement the information content and construct an “image”

617 of the process". Based on the methodology proposed in this paper and the corresponding results,  
618 the following discussion aims to better clarify why we applied an uncoupled approach.

619 Let's refer to the vertical water infiltration process monitored by the EMI sensor during the 1<sup>st</sup>  
620 experiment and producing direct measurements of apparent electrical conductivity ( $\sigma_{a\_meas}$ ). In a  
621 coupled approach, the hydrological model is the starting point of the procedure. Guess values of  
622 hydraulic and dispersive parameters are initially fixed; thus, a hydrological simulation is carried  
623 out producing water content distributions along the soil profile, evolving over time. These water  
624 content distributions are converted to corresponding distributions of bulk electrical conductivity,  
625  $\sigma_b$ , by using an empirical relationship (e.g. Binley et al., 2002). These  $\sigma_b$  distributions, in turn, are  
626 used as input in an EM forward modelling to produce the estimations of apparent electrical  
627 conductivity ( $\sigma_{a\_est}$ ). In this approach, the objective function involves the residuals ( $\sigma_{a\_meas} - \sigma_{a\_est}$ ).  
628 This objective function is eventually minimised by optimising the hydraulic parameters in the  
629 hydrological model.

630 The main strength of this approach relies on the fact that no EMI inversion is required. Also,  
631 as discussed by Hinnell et al. (2010), the attractiveness of the coupled approach is that the  
632 hydrologic model may provide the physical context for a plausible interpretation of the geophysical  
633 measurements. Yet, this strength is counterbalanced by a weakness which is crucial in view of  
634 simplifying the experimental requirements of hydraulic characterization. Actually, an instrumental  
635 shift in EMI  $\sigma_a$  readings has been frequently observed when compared to other sources of  
636 measurements such as ERT data (von Hebel et al., 2014; 2019) or direct measurements of TDR  
637 (Dragonetti et al. 2018). In the context of a hydraulic parameter estimation procedure, this is a  
638 crucial point, as it means that EMI measurements do not immediately provide correct electrical  
639 conductivity distributions. Thus, the coupled approach always requires an independent dataset,

640 obtained by different sensors (e.g. ERT, TDR, sampling) to remove the shift in the EMI  $\sigma_a$   
641 readings. Such a scheme would be contrary to the spirit of [this](#) paper, which mainly aims at  
642 minimising the sensors and the data necessary for in-situ soil hydraulic characterization.

643 In an uncoupled approach, the geophysical model is the starting point of the procedure. As a  
644 result of geophysical inversion, the  $\sigma_b$  distributions are derived, which are then converted to as  
645 many distributions of water content ( $\theta_{meas}$ ) through an empirical relationship, determined from  
646 laboratory analysis. Afterward, the hydrological model estimates water contents ( $\theta_{est}$ ), and the  
647 objective function, involving the residuals ( $\theta_{meas}-\theta_{est}$ ), is eventually minimised by optimising the  
648 hydraulic parameters. The main weakness of this approach corresponds to the strength of the  
649 coupled approach. The uncoupled approach requires geophysical inversion, involving the  
650 uncertainty source coming from the ill-posedness problem. However, the main strength of the  
651 methodology we propose in [this](#) paper – a fast in-situ non-invasive method to estimate soil  
652 hydraulic and transport properties at plot scale – does not require preliminary removal of the  
653 (unknown) shift in the EMI readings by additional field measurements with other sensors.  
654 Conversely, the shift effect is implicitly kept in the  $\sigma_b$  distributions, from this in the measured  
655 water content distributions and finally included in the hydrological inversion. This allowed us to  
656 reveal the effects of technical limitations of the EMI sensor including the instrumental shift in EMI  
657  $\sigma_a$  readings in the water content estimations and from this in the hydraulic properties' estimation.  
658 In the 1<sup>st</sup> experiment, by comparing the EMI-based water contents to the water contents coming  
659 from TDR, it was possible to see that the shift in the EMI readings produced quasi-parallel water  
660 content evolutions, thus meaning that the EMI shift is rather stable with water content change.  
661 Related to this, in terms of hydraulic properties, the shift simply results in scaled saturated water  
662 content. This may well be explained physically by just considering the parallel behaviour of the

663 water contents over time signifies similar water content changes over time. This is translated in  
664 similar hydraulic conductivities, which in the van Genuchten-Mualem model means similar  $\alpha$  and  
665  $n$  parameters, and thus water retention curves are simply scaled by the saturated water content  
666 ratio.

667 As an additional benefit of an uncoupled approach, it allows for the sequential estimation of  
668 parameters (from the upper to the lower horizon), which can reduce the problems of parameter  
669 correlation and uniqueness. In this work, the parameters were estimated separately for each horizon  
670 of the profile according to Abbaspour et al. (1999). This approach makes parameter estimation of  
671 multi-layered profiles more feasible and accurate, however, this cannot be done within a coupled  
672 model. If more than one layer has to be characterised, the coupled approach requires that all the  
673 parameters have to be simultaneously optimised. This is because the electrical conductivity  
674 distribution of the whole soil profile must be first simulated in order to generate required  $\sigma_{a\_est}$  to  
675 compare to  $\sigma_{a\_meas}$  in the objective function.

676

## 677 **5.2. Suitability of EMI as a replacement for invasive sensors**

678 The proposed methodology for the estimation of vG-M parameters proved to be effective for  
679 both Ap and Bw horizons. The overall EMI-based underestimation of  $\theta$  did not impact the  
680 hydraulic conductivity curves significantly, as the [shape of](#) hydraulic conductivity is [mainly](#)  
681 [explained mainly function of by](#) the  $\theta$  variation and not of its absolute value. On the other hand,  
682 this underestimation resulted in lower saturated water content which also appeared in the water  
683 retention curve. The latter can be simply converted to more accurate water content distribution by  
684 direct measurement of the actual saturated water content at the end of the experiment using TDR  
685 probes or even by taking soil samples for laboratory weight.

686 In terms of the longitudinal dispersivity,  $\lambda$ , there was a very good agreement between EMI-  
687 based and TDR-based estimation for both Ap and Bw horizons. The finding results are also in very  
688 good agreement with previous in-situ and laboratory measurements. However, this method  
689 requires that the hydraulic properties of the investigated soil at the scale of concern be assessed  
690 prior to the application of this method to discriminate the contribution of water content and  
691 concentration in the EMI-based  $\sigma_b$  estimation.

692

### 693 **5.3. EMI-related sources of uncertainty**

694 The application of EMI for detailed investigation of the infiltration process has several  
695 limitations, apart from the potential instrumental drift of EMI sensor and the overall  
696 underestimation of water content and concentration, and requires further investigation. Resolving  
697 the wetting zone during the water injection is one source of uncertainty in this approach. The water  
698 content sharply decreases with depth in this zone to near the initial water content of the soil and  
699 causes dramatic resistivity variation. The limited number of  $\sigma_a$  measurements (total of 6) is not  
700 sufficient for recovering the sharp  $\sigma_b$  variability that takes place during the infiltration. In addition,  
701 a smoothness constraint was performed in the inversion process to stabilize the inversion process  
702 which further smooths the layer boundaries in this approach. Resolving the shallow bedrock  
703 interface at depth and beneath a conductive zone was also very challenging. This is because the  
704 sensitivity of the EMI signals is generally very limited over the resistive zone and the condition  
705 becomes much worse when the resistive zone (bedrock) is located beneath a conductive zone  
706 (tracer): the EMI response of the subsurface is dominated by the influence of the near-surface  
707 conductive zone. In addition, five of the six depths of investigation of the CMD Mini-Explorer are  
708 limited to the first 1 m, and, as a result, a lower resolution is expected at greater depths. This  
709 resulted in an even larger underestimation of soil conductivity on top of the bedrock and an

710 overestimation of bedrock conductivity in the close vicinity of soil. These findings from synthetic  
711 studies and modelling field data are similar to those reported in Farzamian et al. (2021) due to the  
712 similarity of the site, experiment, and the use of the same EMI sensor. Measuring  $\sigma_a$  at different  
713 heights or using different EMI sensor with larger number of receivers such as CMD Mini-Explorer  
714 6L enables us to collect more  $\sigma_a$  data to better resolve changes that occur over short depth  
715 increments. To this aim, the EMI configuration and data survey can also be optimized using  
716 optimization techniques such as machine learning based methods, given the specific survey goals  
717 and independent knowledge of the subsurface electrical properties, as shown for example by van't  
718 Veen et al. (2022).

719

## 720 **6. CONCLUSION**

721 In this paper, we proposed a non-invasive in-situ method integrating EMI and hydrological  
722 modelling to estimate soil hydraulic and transport properties at the plot scale. For this purpose, we  
723 carried out two experiments involving 1) water infiltration and 2) solute transport over a 4 x 4 m  
724 plot. The propagation of wetting front and solute concentration along the soil profile in the plot  
725 was monitored using an EMI sensor (i.e. CMD mini-Explorer) and for the sake of procedure  
726 evaluation Time Domain Reflectometry probes and tensiometers. Time-lapse apparent electrical  
727 conductivity ( $\sigma_a$ ) data obtained from the EMI sensor were inverted to estimate the evolution over  
728 time of the vertical distribution of the bulk electrical conductivity ( $\sigma_b$ ). The  $\sigma_b$  distributions were  
729 converted to water content and solute concentration by using a standard laboratory calibration,  
730 relating  $\sigma_b$  to water content ( $\theta$ ) and soil solution electrical conductivity ( $\sigma_w$ ).

731 Based on the first water infiltration experiment, the soil water retention and hydraulic  
732 conductivity curves were then obtained for two layers of the soil profile by an optimization

733 procedure minimizing the deviations between the numerical solution of the water infiltration  
734 experiment and the estimated water contents inferred from the EMI results. EMI-based hydraulic  
735 properties were very similar in shape to those obtained by TDR and tensiometers data. This shape-  
736 similarity allowed to convert the EMI-based hydraulic properties to the TDR-based ones by simply  
737 scaling them by the ratio of the saturated water content for both the soil layers considered. This  
738 was a crucial finding in this paper and was mainly ascribed to the fact that the water content  
739 changes over time detected by the EMI closely followed those observed by TDR. These EMI-  
740 based hydraulic properties were then used as input for hydrological modelling of the second solute  
741 transport experiment. This allowed discriminating water content and solute concentration  
742 components in the EMI  $\sigma_b$  distributions obtained during the second experiment. These  
743 concentrations were afterward used to estimate the dispersivity based on an inversion procedure  
744 minimizing the residuals of EMI-based concentration and those simulated by the hydrological  
745 model. The reliability of the EMI-based hydraulic properties allowed us to obtain estimations of  
746 the dispersivity comparable to those obtained by the same optimization procedure applied to the  
747 TDR data.

748 The overall results show the high potential of the EMI sensor to replace TDR and tensiometer  
749 probes in the assessment of soil hydraulic properties. In practice, one could monitor a relatively  
750 short infiltration experiment with an EMI sensor and use the water content estimations in an  
751 inversion procedure to estimate the hydraulic properties. The underestimated water content  
752 observed in the first experiment can be converted to more accurate water content distribution by  
753 direct measurement of the actual saturated water content at the end of the experiment using TDR  
754 probes or even by taking samples and laboratory measurements.



755 The EMI-based estimation of longitudinal dispersivity,  $\lambda$  agrees well with TDR-based  
756 estimation as well as previous in-situ and laboratory measurements which suggests that the  
757 proposed methodology can be used in the assessment of this parameter which is indeed an  
758 important parameter in soil salinity simulations in salt-affected regions across the world. However,  
759 estimating  $\lambda$  based on only a solute infiltration test is not feasible as the temporal variability of  $\sigma_b$   
760 is a function of both water content and concentration changes. We proposed the sequence of water  
761 and solute infiltration tests to discriminate the contribution of the water content and the soil  
762 solution electrical conductivity to the EMI-based  $\sigma_b$ .

763 Water irrigation and soil salinity management and thus hydrological investigations are usually  
764 field and even large-scale challenges. The EM method is a non-invasive, fast, and cost-effective  
765 technique, covering large areas in less time and at a lower cost. Although ~~our~~[this](#) study was limited  
766 to a controlled experiment on a plot scale and a single study report, scaling up from plot scale to  
767 field scale assessment might be feasible due to the method's potential for rapid data collection.  
768 More investigations have to be conducted in this area to evaluate the potential of EMI sensors  
769 under different soil conditions and within the larger 2D and 3D investigations to further address  
770 the limitations of this methodology at different scales.

771

## 772 **ACKNOWLEDGMENTS**

773 This work was funded in the scope of the project SALTFREE: Salinization in irrigated areas: risk  
774 evaluation and prevention [ARIMNet2, Grant agreement no. 618127], by the Italian Ministry of  
775 Agricultural, Food and Forestry Policies [D.M. 28675/7303/15]. M. Farzamian was supported by

776 a contract within project SOIL4EVER [Increasing water productivity through the sustainable use  
777 of soils, PTDC/ASP-SOL/28796/2017].

778

779 **REFERENCES**

780 Abbasi, F., Šimůnek, J., Feyen, J., van Genuchten, M.T., and Shouse, P.T.: Simultaneous inverse  
781 estimation of soil hydraulic and solute transport parameters from transient field experiments:  
782 Homogeneous soil. *Transactions of the ASAE* 46(4): 1085, 2003.

783 Abbaspour, K.C., Sonnleitner, M., and Schulin, R.: Uncertainty in estimation of soil hydraulic  
784 parameters by inverse modeling: example lysimeter experiments. *Soil Sci. Soc. Am. J.* 63, 501–  
785 509, 1999.

786 Archie, G.E.: The electrical resistivity log as an aid in determining some reservoir characteristics.  
787 *Transactions of the AIME* 146(01): 54–62, 1942.

788 Basile, A., Coppola, A., De Mascellis, R., and Randazzo, L.: Scaling Approach to Deduce Field  
789 Unsaturated Hydraulic Properties and Behavior from Laboratory Measurements on Small  
790 Cores, *Vadose Zone J.*, 5, 1005–1016, <https://doi.org/10.2136/vzj2005.0128>, 2006.

791 Binley, A., Cassiani, G., Middleton, R., and Winship, P.: Vadose zone flow model  
792 parameterisation using cross-borehole radar and resistivity imaging. *Journal of Hydrology*  
793 267(3–4): 147–159, [https://doi.org/10.1016/S0022-1694\(02\)00146-4](https://doi.org/10.1016/S0022-1694(02)00146-4), 2002.

794 Bouksila, F., Persson, M., Bahri, A., and Berndtsson, A.: Electromagnetic induction prediction of  
795 soil salinity and groundwater properties in a Tunisian Saharan oasis. *Hydrological sciences*  
796 *journal* 57(7): 1473–1486, <https://doi.org/10.1080/02626667.2012.717701>. 2012.

797 Camporese, M., Cassiani G., Deiana R., Salandin P., and Binley A.: Coupled and uncoupled  
798 hydrogeophysical inversions using ensemble Kalman filter assimilation of ERT-monitored  
799 tracer test data, *Water Resour. Res.*, 51, 3277–3291, doi:10.1002/2014WR016017, 2015

800 Caputo, M.C., De Carlo, L., Masciopinto, C., and Nimmo, J.R.: Measurement of field-saturated  
801 hydraulic conductivity on fractured rock outcrops near Altamura (Southern Italy) with an  
802 adjustable large ring infiltrometer, *Environ. Earth Sci.*, 60, 583–590,  
803 <https://doi.org/10.1007/s12665-009-0198-y>, 2010.

804 Caputo M.C., Maggi S., and Turturro A.C.: Calculation of Water Retention Curves of Rock  
805 Samples by Differential Evolution, in: *Engineering Geology for Society and Territory*, edited  
806 by Lollino G., Manconi A., Guzzetti F., Culshaw M., Bobrowsky P., Luino F. (eds), Volume 5,  
807 Springer, Cham, <https://doi.org/10.1007/978-3-319-09048-1>, 2015.

808 Coppola, A., Comegna, A., Dragonetti, G., Dyck, M., Basile, A., Lamaddalena, N., Kassab, M.,  
809 and Comegna, V.: Solute transport scales in an unsaturated stony soil, *Adv. Water Resour.*, 34,  
810 747–759, <https://doi.org/10.1016/j.advwatres.2011.03.006>, 2011.

811 Coppola, A., Gerke, H., Comegna, A., Basile, A., and Comegna, V.: Dual-permeability model for

812 flow in shrinking soil with dominant horizontal deformation. *Water Resources Research*, Vol.  
813 48, W08527, doi:10.1029/2011WR011376, 2012.

814 Coppola, A., Smettem, K., Ajeel, A., Saeed, A., Dragonetti, G., Comegna, A., Lamaddalena, N.,  
815 and Vacca, A.: Calibration of an electromagnetic induction sensor with time-domain  
816 reflectometry data to monitor rootzone electrical conductivity under saline water irrigation, *Eur.*  
817 *J. Soil Sci.*, 67, 737–748, <https://doi.org/10.1111/ejss.12390>, 2016.

818 Coppola, A., Dragonetti, G., Comegna, A., Lamaddalena, N., Caushi, B., Haikal, M. A., and  
819 Basile, A.: Measuring and modeling water content in stony soils, *Soil and Tillage Research*,  
820 128, 9–22, <https://doi.org/10.1016/j.still.2012.10.006>, 2013.

821 Coppola, A., Dragonetti, G., Sengouga, A., Lamaddalena, N., Comegna, A., Basile, A., Noviello,  
822 N., and Nardella, L.: Identifying Optimal Irrigation Water Needs at District Scale by Using a  
823 Physically Based Agro-Hydrological Model. *Water* 11(4). <https://doi.org/10.3390/w11040841>,  
824 2019.

825 Coppola, A., Chaali, N., Dragonetti, G., Lamaddalena, N., and Comegna, A.: Root uptake under  
826 non-uniform root-zone salinity, *Ecohydrology*, 8, 1363–1379,  
827 <https://doi.org/10.1002/eco.1594>, 2015.

828 Corwin, D. L., and Lesch, S. M.: Apparent soil electrical conductivity measurements in agriculture,  
829 *Comput. Electron. Agr.*, 46, 11–43, <https://doi.org/10.1016/j.compag.2004.10.005>, 2005.

830 Dane, J. H., & Topp, C. G. (Eds.). (2020). *Methods of soil analysis, Part 4: Physical methods (Vol.*  
831 *20)*. John Wiley & Sons.

832 Deidda, G.P., Fenu, C., and Rodriguez, G.: Regularized solution of a nonlinear problem in  
833 electromagnetic sounding, *Inverse Probl.*, 30, 125014, <https://doi.org/10.1088/0266-5611/30/12/125014>, 2014.

835 Dragonetti, G., Comegna, A., Ajeel, A., Deidda, G. P., Lamaddalena, N., Rodriguez, G., Vignoli,  
836 G., and Coppola, A.: Calibrating electromagnetic induction conductivities with time-domain  
837 reflectometry measurements, *Hydrol. Earth Syst. Sci.*, 22, 1509–1523,  
838 <https://doi.org/10.5194/hess-22-1509-2018>, 2018.

839 Ellsworth, T.R., Shaouse, P.J., Jobes, J.A., Fargerlund, J., and Skaggs, T.H.: Solute transport in  
840 unsaturated soil: Experimental design, parameter estimation, and model discrimination. *Soil*  
841 *Science Society of America Journal* 60(2): 397–407,  
842 <https://doi.org/10.2136/sssaj1996.03615995006000020010x>, 1996.

843 Farzamian, M., Paz, M. C., Paz, A. M., Castanheira, N. L., Gonçalves, M. C., Monteiro Santos, F.  
844 A., and Triantafilis, J.: Mapping soil salinity using electromagnetic conductivity imaging—A  
845 comparison of regional and location-specific calibrations, *Land. Degrad. Dev.*, 30, 1393–1406,  
846 <https://doi.org/10.1002/ldr.3317>, 2019a.

847 Farzamian, M., Ribeiro, J.A., Monteiro Santos, F.A., Khalil M.A.: Application of Transient  
848 Electromagnetic and Audio-Magnetotelluric Methods for Imaging the Monte Real Aquifer in  
849 Portugal. *Pure Appl. Geophys*, <https://doi.org/10.1007/s00024-018-2030-7>, 2019b.

850 Farzamian, M., Autovino, D., Basile, A., De Mascellis, R., Dragonetti, G., Monteiro Santos, F.,  
851 Binley, A., and Coppola, A.: Assessing the dynamics of soil salinity with time-lapse inversion  
852 of electromagnetic data guided by hydrological modelling, *Hydrol. Earth Syst. Sci.*, 25, 1509–

853 1527, <https://doi.org/10.5194/hess-25-1509-2021>, 2021.

854 Groh, J., Stumpp, C., Lücke, A., Pütz, T., Vanderborght, J., Vereecken, H.: Inverse estimation of  
855 soil hydraulic and transport parameters of layered soils from water stable isotope and lysimeter  
856 data. *Vadose Zone Journal* 17(1): 1–19, <https://doi.org/10.2136/vzj2017.09.0168>, 2018.

857 Gómez Flores, J.L., Ramos Rodríguez, M., González Jiménez, A., Farzamian, M., Herencia Galán,  
858 J.F., Salvatierra Bellido, B., Cermeño Sacristan, P., and Vanderlinden, K.: Depth-Specific Soil  
859 Electrical Conductivity and NDVI Elucidate Salinity Effects on Crop Development in  
860 Reclaimed Marsh Soils. *Remote Sens.*, 14, 3389. <https://doi.org/10.3390/rs14143389>, 2022.

861 Hansen, S., Abrahamsen, P., Petersen, C.T., Styczen, M., 2012. Daisy: model use, calibration and  
862 validation. *Trans. ASABE* 55, 1315–1333.

863 Hendrickx, J.M.H., Borchers, B., Corwin, D.L., Lesch, S.M., Hilgendorf, A.C., and Schlue, J.:  
864 Inversion of soil conductivity profiles from electromagnetic induction measurements, *Soil Sci.*  
865 *Soc. Am. J.*, 66, 673–685, <https://doi.org/10.2136/sssaj2002.6730>, 2002.

866 Hinnell, A.C., Ferre, T.P.A., Vrugt, J.A., Huisman, J.A., Moysey, S., Rings, J., and Kowalsky,  
867 M.B.: Improved extraction of hydrologic information from geophysical data through coupled  
868 hydrogeophysical inversion. *J. Water Resour. Res.* 46, W00D40,  
869 <https://doi.org/10.1029/2008WR007060>, 2010.

870 Huang, J., Monteiro Santos, F. A., and Triantafyllis, J.: Mapping soil water dynamics and a moving  
871 wetting front by spatiotemporal inversion of electromagnetic induction data, *Water Resour.*  
872 *Res.*, 52, 9131–9145, <https://doi.org/10.1002/2016WR019330>, 2016.

873 Inoue, M., Šimuunek, J., Shiozawa, S., and Hopmans, J.W.: Simultaneous estimation of soil  
874 hydraulic and solute transport parameters from transient infiltration experiments. *Advances in*  
875 *Water Resources* 23(7): 677–688, [https://doi.org/10.1016/S0309-1708\(00\)00011-7](https://doi.org/10.1016/S0309-1708(00)00011-7), 2000.

876 Kaufman, A.A., and Keller, G.V.: *Frequency and Transient Sounding Methods Geochemistry and*  
877 *Geophysics*. Elsevier Science Ltd, New York, 1983.

878 Kemna, A., Vanderborght, J., Kulesa, B., and Vereecken, H.: Imaging and characterization of  
879 subsurface solute transport using electrical resistivity tomography (ERT) and equivalent  
880 transport models. *Journal of hydrology* 267(3–4): 125–146, [https://doi.org/10.1016/S0022-1694\(02\)00145-2](https://doi.org/10.1016/S0022-1694(02)00145-2), 2002.

882 Kroes, J.G., van Dam, J.C., Bartholomeus, R.P., Groenendijk, P., Heinen, M., Hendriks, R. F.A.,  
883 Mulder, H.M., Supit, I., van Walsum, P.E.V., 2017. SWAP version 4; Theory description and  
884 user manual. Wageningen, Wageningen Environmental Research, Report 2780. 244 pp.

885 Lavoué, F., van der Kruk, J., Rings, J., André, F., Moghadas, D., Huisman, J.A., Lambot, S.,  
886 Weihermüller, L., Vanderborght, J., and Vereecken, H.: Electromagnetic induction calibration  
887 using apparent electrical conductivity modelling based on electrical resistivity tomography,  
888 *Near Surf. Geophys.*, 8, 553–561, 2010.

889 Malicki, M. A. and Walczak, R. T.: Evaluating soil salinity status from bulk electrical conductivity  
890 and permittivity, *Eur. J. Soil Sci.*, 50, 505–514, <https://doi.org/10.1046/j.1365-2389.1999.00245.x>, 1999.

892 McLachlan, P., Blanchy, G., and Binley, A.: EMagPy: Open-source standalone software for  
893 processing, forward modeling and inversion of electromagnetic induction data. *Computers &*

894 Geosciences. <https://doi.org/10.1016/j.cageo.2020.104561>, 2020.

895 McNeill, J.D.: Electromagnetic Terrain Conductivity Measurement at Low Induction Numbers.  
896 Geonics Limited, Ontario, Canada, Technical note TN-06 1–15, 1980.

897 Moghadas, D.: Probabilistic Inversion of Multiconfiguration Electromagnetic Induction Data  
898 Using Dimensionality Reduction Technique: A Numerical Study, *Vadose Zone J.*, 18, 1–16,  
899 <https://doi.org/10.2136/vzj2018.09.0183>, 2019.

900 Monteiro Santos, F. A.: 1D laterally constrained inversion of EM34 profiling data, *J. Appl.*  
901 *Geophys.*, 56, 123–134, <https://doi.org/10.1016/j.jappgeo.2004.04.005>, 2004.

902 Paz, M. C., Farzamian, M., Paz, A. M., Castanheira, N. L., Gonçalves, M. C., and Monteiro Santos,  
903 F.: Assessing soil salinity using time-lapse electromagnetic conductivity imaging, *SOIL*, 6,  
904 499–511, <https://doi.org/10.5194/soil-6-499-2020>, 2020.

905 Robinson, D.A., Jones, S.B., Wraith, J.M., Or, D., and Friedman, S.P.: A Review of Advances in  
906 Dielectric and Electrical Conductivity Measurement in Soils Using Time Domain  
907 Reflectometry. *Vadose Zone Journal* 2: 444–475. doi: 10.2136/vzj2003.4440, 2003.

908 Saeed A., Comegna, A., Dragonetti, G., Lamaddalena, N., and Coppola, A.: Soil surface electrical  
909 conductivity estimated by TDR and EMI sensors: Accounting for the different sensor  
910 observation volumes, *J. of Agricultural Engineering*. Vol XLVIII, doi:10.4081/jae.2017.716,  
911 2017.

912 Sasaki, Y.: Full 3-D inversion of electromagnetic data on PC. *Journal of Applied Geophysics*  
913 46(1): 45–54. doi: 10.1016/S0926-9851(00)00038-0, 2001.

914 Severino G, Comegna A., Coppola A., Sommella A., Santini A.: Stochastic analysis of a field-  
915 scale unsaturated transport experiment, *Advances in Water Resources*,  
916 doi:10.1016/j.advwatres.2010.09.004, 2010.

917 Šimůnek, J., Angulo-Jaramillo, R., Schaap, M.G., Vandervaere, J.P., and van Genuchten, M.T.:  
918 Using an inverse method to estimate the hydraulic properties of crusted soils from tension-disc  
919 infiltrometer data. *Geoderma* 86(1): 61–81. doi: 10.1016/S0016-7061(98)00035-4, 1998a.

920 Šimůnek, J., Sejna, M., van Genuchten, M.T., Šimuunek, J., and Šejna, M.: HYDRUS-1D.  
921 Simulating the one-dimensional movement of water, heat, and multiple solutes in variably-  
922 saturated media, version 2, 1998b.

923 Sisson, J., and van Genuchten, M.Th.: An improved analysis of gravity drainage experiments for  
924 estimating the unsaturated soil hydraulic functions. *Water Resour. Res.* 27:569–575, 1991.

925 Singha, K., and Gorelick, S.M.: Saline tracer visualized with three-dimensional electrical  
926 resistivity tomography: Field-scale spatial moment analysis. *Water Resources Research* 41(5).  
927 <https://doi.org/10.1029/2004WR003460>, 2005.

928 Topp, G.C., Davis, J.L., and Annan, A.P.: Electromagnetic determination of soil water content:  
929 Measurements in coaxial transmission lines. *Water Resources Research*, 16(3), 574–582, 1980.

930 Vanderborght J., and Vereecken, H.: Review of Dispersivities for Transport Modeling in Soils.  
931 *Vadose Zone Journal* 6(1) doi:10.2136/vzj2006.0096, 2007.

932 Watson, K. K., 1966. An instantaneous profile method for determining the hydraulic conductivity  
933 of unsaturated porous materials, *Water Resour. Res.*, 2, 709–715, 1966.

- 934 van Genuchten, M. T.: A closed-form equation for predicting the hydraulic conductivity of  
935 unsaturated soils, *Soil Sci. Soc. Am. J.*, 44, 892–898, 1980.
- 936 van Genuchten, M.T., Leij, F.J. and Wu, L.: Characterization and measurement of the hydraulic  
937 properties of unsaturated porous media (parts 1 and 2). *Proceedings of the International*  
938 *Workshop, Riverside, Calif., 22--24 Oct, 1999.*
- 939 van't Veen, K.M., Ferré, T.P.A., Iversen, B.V., and Børgesen, C.D.: Using machine learning to  
940 predict optimal electromagnetic induction instrument configurations for characterizing the  
941 shallow subsurface, *Hydrol. Earth Syst. Sci.*, 26, 55–70, [https://doi.org/10.5194/hess-26-55-](https://doi.org/10.5194/hess-26-55-2022)  
942 [2022](https://doi.org/10.5194/hess-26-55-2022), 2022.
- 943 Visconti, F., and de Paz, J.M.: Sensitivity of soil electromagnetic induction measurements to  
944 salinity, water content, clay, organic matter and bulk density. *Precision Agriculture*, 2021,1-19,  
945 doi: 10.1007/s11119-021-09798-8, 2021.
- 946 von Hebel, C., Rudolph, S., Mester, A., Huisman, J. A., Kumbhar, P., Vereecken, H., and van der  
947 Kruk, J.: Three-dimensional imaging of subsurface structural patterns using quantitative large-  
948 scale multiconfiguration electromagnetic induction data, *Water Resour. Res.*, 50, 2732–2748,  
949 <https://doi.org/10.1002/2013WR014864>, 2014.
- 950 von Hebel, C., van der Kruk, J., Huisman, J.A., Mester, A., Altdorff, D., Endres, A.L.,  
951 Zimmermann, E., Garré, S., and Vereecken, H.: Calibration, Conversion, and Quantitative  
952 Multi-Layer Inversion of Multi-Coil Rigid-Boom Electromagnetic Induction Data. *Sensors*, 19,  
953 4753. <https://doi.org/10.3390/s19214753>, 2019.
- 954 Wessolek, G., Plagge, R. Leij, F.J., and van Genuchten, M.T.: Analysing problems in describing  
955 field and laboratory measured soil hydraulic properties. *Geoderma* 64(1–2): 93–110.  
956 [https://doi.org/10.1016/0016-7061\(94\)90091-4](https://doi.org/10.1016/0016-7061(94)90091-4), 1994.
- 957 Whalley, W. R., Binley, A. M., Watts, C. W., Shanahan, P., Dodd, I. C., Ober, E. S., Ashton, R.  
958 W., Webster, C. P., White, R. P., and Hawkesford, M. J.: Methods to estimate changes in soil  
959 water for phenotyping root activity in the field, *Plant Soil*, 415, 407–422.  
960 <https://doi.org/10.1007/s11104-016-3161-1>, 2017.
- 961 Zare, E., Li, N., Khongnawang, T., Farzamian, M., and Triantafilis, J.: Identifying Potential  
962 Leakage Zones in an Irrigation Supply Channel by Mapping Soil Properties Using  
963 Electromagnetic Induction, Inversion Modelling and a Support Vector Machine, *Soil Syst.*, 4,  
964 25, <https://doi.org/10.3390/soilsystems4020025>, 2020.